J. Fluid Mech. (2009), *vol.* 639, *pp.* 101–131.
doi:10.1017/S0022112009990814

Structures in turbulent boundary layers subjected to adverse pressure gradients

JOUNG-HO LEE AND HYUNG JIN SUNG†

Department of Mechanical Engineering, KAIST, 335 Gwahangno,
Yuseong-Gu 305-701, Republic of Korea

(Received 15 November 2008; revised 14 June 2009; accepted 14 June 2009)

The effects of adverse pressure gradients on turbulent structures were investigated by carrying out direct numerical simulations of turbulent boundary layers subjected to adverse and zero pressure gradients. The equilibrium adverse pressure gradient flows were established by using a power law free-stream distribution $U_\infty \sim x^m$. Two-point correlations of velocity fluctuations were used to show that the spanwise spacing between near-wall streaks is affected significantly by a strong adverse pressure gradient. Low-momentum regions are dominant in the middle of the boundary layer as well as in the log layer. Linear stochastic estimation was used to provide evidence for the presence of low-momentum regions and to determine their statistical properties. The mean width of such large-scale structures is closely associated with the size of the hairpin-like vortices in the outer layer. The conditionally averaged flow fields around events producing Reynolds stress show that hairpin-like vortices are the structures associated with the production of outer turbulence. The shapes of the vortices beyond the log layer were found to be similar when their length scales were normalized according to the boundary layer thickness. Estimates of the conditionally averaged velocity fields associated with the spanwise vortical motion were obtained by using linear stochastic estimation. These results confirm that the outer region of the adverse pressure gradient boundary layer is populated with streamwise-aligned vortex organizations, which are similar to those of the vortex packet model proposed by Adrian, Meinhart & Tomkins (*J. Fluid Mech.*, vol. 422, 2000, pp. 1–54). The adverse pressure gradient augments the inclination angles of the packets and the mean streamwise spacing of the vortex heads in the packets.

1. Introduction

Turbulent boundary layers (TBLs) are subjected to adverse pressure gradients (APGs) in numerous engineering applications, such as diffusers, turbine blades and the trailing edges of aerofoils. The upper limit of the efficiency of such devices is almost always determined by the APG, so the behaviour of the APG flows is of practical importance. Understanding the coherent structures in TBLs is essential to understanding boundary layer turbulence. Since organized motions play a crucial role in the production and dissipation of wall turbulence, the study of coherent structures contributes to the accuracy of turbulence models (Aubry *et al.* 1988) and advances in flow control strategies (Robinson 1991). Therefore, elucidating the behaviour of the

† Email address for correspondence: hjsung@kaist.ac.kr

coherent structures in APG TBLs provides insight into the physics of the APG flow and improves its modelling.

Most previous studies of organized motions have been carried out for a zero pressure gradient (ZPG) boundary layer and flow bounded by a smooth wall and have focused on the near-wall region. In a flow visualization study of ZPG TBLs, Kline *et al.* (1967) found that low-speed streaks are present in the sublayer and that the mean spanwise spacing between the streaks is approximately 100 viscous wall units. Kline & Robinson (1989) and Jeong *et al.* (1997) observed that quasi-streamwise vortices are predominant in the buffer regions of TBLs. It is widely accepted that near-wall streaks and quasi-streamwise vortical structures are the most significant structures in TBLs and that they are responsible for most turbulence production near walls.

Much effort has recently been devoted to investigating the outer structures of TBLs, especially with regard to the role of hairpin packets. Adrian (2007) has provided a comprehensive review of these studies. Theodorsen (1952) was the first to propose a hairpin model. Throughout this paper, 'hairpin vortex' is used to describe both asymmetric and symmetric hairpins that have the shape of an arch, a horseshoe, a hairpin and a cane-shaped vortex. Bandyopadhyay (1980) and Head & Bandyopadhyay (1981) performed smoke flow visualizations of ZPG TBLs and found groups of hairpin structures in boundary layers with low to high Reynolds numbers. Smith *et al.* (1991) proposed the theoretical mechanism on the basis of their previous experimental results (Acarlar & Smith 1987) that successive in-line hairpins could be formed. Zhou *et al.* (1999) performed a direct numerical simulation (DNS) of the evolution of a hairpin vortex to explore the formation mechanism of hairpins in packets. They suggested that any primary hairpin with a vorticity above a threshold strength autogenerates new hairpin vortices both upstream and downstream of the initial hairpin.

Recent high-resolution velocity field measurements with particle image velocimetry (PIV) have shown that hairpin vortices are commonly observed in logarithmic layers and in the wake regions of TBLs (Adrian *et al.* 2000). These vortices form packets and convect with nearly the same velocities. Christensen & Adrian (2001) carried out linear stochastic estimations (LSEs) that supported the observations of Adrian *et al.* (2000). A streamwise series of hairpins was found to induce low-speed flows (Adrian *et al.* 2000; Tomkins & Adrian 2003). A PIV study carried out by Ganapathisubramani, Longmire & Marusic (2003) demonstrated that such outer low-speed streaky structures and hairpin vortex packets create most of the mean Reynolds shear stress in the outer layer. Marusic (2001) concluded that the packet model can be used to generate turbulence statistics that are better than those provided by the randomly scattered hairpin model (Perry, Henbest & Chong 1986). This result confirms the presence and importance of hairpin packets in ZPG TBLs.

Many important features of APG TBLs are quite well understood. In general, as the magnitude of the APG increases, the mean velocity profile develops a large wake region and the turbulent kinetic energy decreases in the near-wall region (Nagano, Tagawa & Tsuji 1993). In an experimental study of an APG TBL near separation, Skåre & Krogstad (1994) found that the statistics in the outer layer are significantly affected by a strong APG. In particular, there is an outer peak in the Reynolds shear stress in the outer layer due to the APG. Further, there is an outer peak in the production term of the turbulent kinetic energy that is due to the peak in the Reynolds shear stress. A recent DNS study of APG TBLs by Lee & Sung (2008) has supported the conclusions of previous experiments (Nagano *et al.* 1993; Skåre &

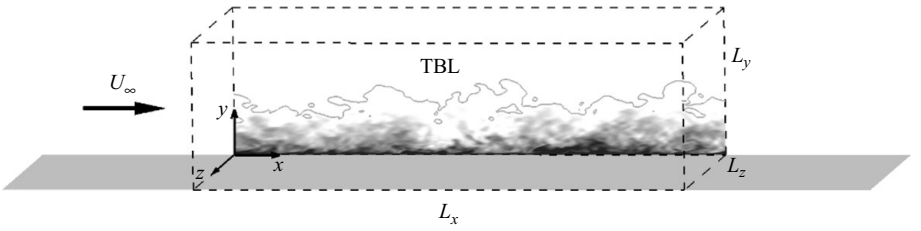

FIGURE 1. Schematic diagram of the computational domain and coordinate system.

Krogstad 1994), in particular that the production of turbulence in the outer layer is as significant as near-wall turbulence.

Little is known about the effects of APGs on coherent structures in TBLs. Krogstad & Skåre (1995) studied the structures in a TBL subjected to a strong APG. By using two-point velocity correlations, they showed that the streamwise correlation length of the streamwise velocity decreases when a strong APG is applied but that the inclination angles of the correlations in the outer layers of the APG and ZPG flows are similar. Marusic & Perry (1995) and Perry & Marusic (1995) extended the attached-eddy hypothesis, based on the idea of Townsend, to APG TBLs by making the assumption that each individual eddy is independent of the pressure gradient. The randomly scattered hairpin model can be used to reproduce many statistical properties of ZPG TBLs. However, they found that hairpin-type eddy models fail to reconstruct the shear stress distributions in the outer layers of several different APG boundary layers and concluded that large-scale eddies must be taken into account to predict the properties of the APG flows. In a DNS study of low-Reynolds-number APG TBLs, Skote, Henningson & Henkes (1998) proposed that enhanced outer turbulence is associated with outer streaky structures. Although the evidence for large-scale structures in the APG flows is strong, relatively little information about the physics of such flow structures in APG TBLs is available.

The main objective of this study was to examine statistically the effects of APGs on the coherent structures of TBLs. We used LSE (Adrian *et al.* 1989) to investigate the conditionally averaged vortical structures in various APG TBLs. The DNS database of TBLs with APGs generated by Lee & Sung (2008) was analysed. The streamwise variation of the free-stream velocity must have the form of a power law relation $U_\infty \sim x^m$ to produce an equilibrium TBL (Townsend 1961; Mellor & Gibson 1966).

A schematic diagram of the computational domain is shown in figure 1. To investigate the effects of APGs, simulations were performed using two values of m, -0.15 and -0.2, representing moderate and strong APGs respectively. For comparison, a ZPG TBL ($m = 0$) was also simulated. Most comparison of the statistics was made in the equilibrium region. The instantaneous flow fields were analysed to characterize the responses of the turbulent structures to the APGs. Two-point correlations and LSE were used to determine the statistical properties of the low-momentum regions (LMRs) and of individual vortices. Vortex packet characteristics were obtained by using flow visualization. Finally, the conditionally averaged velocity fields associated with transverse swirling motions were extracted by using LSE in order to investigate the characteristics of the organized motions statistically.

m	Δx^+	Δy^+_{min}	Δy^+_{max}	Δz^+	Δt^+	$L_x/\theta_{in} \times L_y/\theta_{in} \times L_z/\theta_{in}$	Grid
0	15	0.2	40	5	0.2	$240 \times 30 \times 40$	$1025 \times 161 \times 513$
−0.15	12.5	0.17	24	5	0.25	$1600 \times 80 \times 80$	$2049 \times 121 \times 257$
−0.2	12.5	0.17	24	5	0.25	$1600 \times 120 \times 160$	$2049 \times 161 \times 513$

TABLE 1. Simulation details.

2. Computational details

The governing equations were integrated in time by using the fractional step method with the implicit velocity decoupling procedure proposed by Kim, Baek & Sung (2002). In this approach, the terms are first discretized in time with the Crank–Nicolson method, and then the coupled velocity components in the convection terms are decoupled with the implicit velocity decoupling procedure. The overall accuracy in time was second-order. All of the terms were resolved with a second-order central difference scheme in space by using a staggered mesh. The domain size and the spatial and time resolutions in wall units are summarized in table 1. The streamwise resolution ($\Delta x^+ \approx 12.5$) for APG was comparable to the one used in DNSs of APG boundary layer flows performed earlier, $\Delta x^+ \approx 13$ (Skote *et al.* 1998) and $\Delta x^+ \approx 16.6$ (Na & Moin 1998). The total simulation time was 4900, 15 000 and 30 000 θ_{in}/U_0, and averaging time for turbulent statistics was 3500, 9000 and 24 000 θ_{in}/U_0 for the case of $m = 0$, -0.15 and -0.2 respectively. Statistical quantities were averaged over time and the spanwise direction.

Time-dependent ZPG turbulent inflow data at the inlet were generated with the method of Lund, Wu & Squires (1998). The Reynolds numbers at the inlet were 300 for the APG flows and 1410 for the ZPG flow. A convective boundary condition of the form $(\partial u/\partial t)+c(\partial u/\partial x) = 0$, where c is the local bulk velocity, was applied at the exit; this boundary condition allows propagating vortex structures to exit the domain with minimum distortion. The no-slip condition was imposed at the solid wall. Periodic boundary conditions were applied in the spanwise direction. The free-stream velocity U_∞ along the upper boundary of the computational domain was specified as

$$\left.\begin{aligned} u = U_\infty(x) &= \begin{cases} U_0 & \text{for } x < 0, \\ U_0\left(1 - \frac{x}{x_0}\right)^m & \text{for } x \geqslant 0, \end{cases} \\ \frac{\partial v}{\partial y} &= -\frac{\partial u}{\partial y}, \\ \frac{\partial w}{\partial y} &= 0, \end{aligned}\right\} \tag{2.1}$$

where m denotes the exponent of the APG. Three cases ($m = 0$, -0.15 and -0.2) were investigated (figure 2), which correspond to a ZPG ($\beta = 0$) and moderate ($\beta = 0.73$) and strong ($\beta = 1.68$) APGs, respectively. The non-dimensionalized pressure gradient parameter β is defined as $(\delta^*/\tau_w)\mathrm{d}P/\mathrm{d}x$. Here, δ^* is the displacement thickness and τ_w is the wall shear stress. Figure 3 shows the location of the equilibrium region. The values of Clauser's parameters and the Reynolds number ranges in the equilibrium region are listed in table 2. To ascertain the reliability and accuracy of these numerical simulations, we compared the turbulence statistics for the ZPG case ($m = 0$) with the experimental data of De Graaf & Eaton (2000) (see figure 4). The mean velocity and

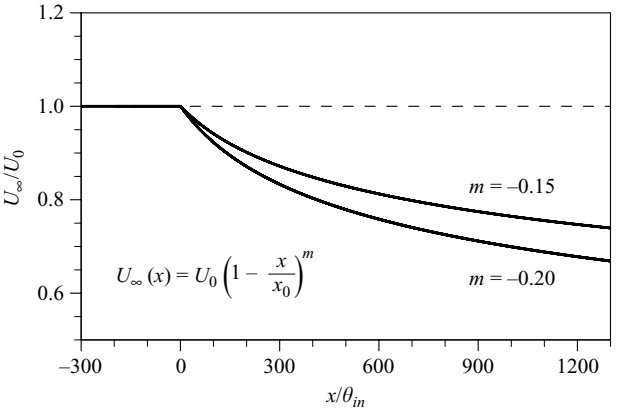

FIGURE 2. Free-stream velocity distribution along the upper boundary of the computational domain.

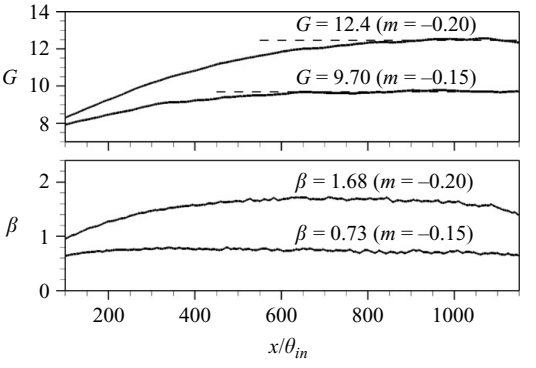

FIGURE 3. Clauser's equilibrium parameters: non-dimensionalized pressure gradient parameters β and G.

m	β	G	Re_θ
—0.15	0.73	9.70	1000–1300
—0.20	1.68	12.4	1200–1400

TABLE 2. Flow parameters.

turbulence intensities we obtained are in good agreement with those of De Graaf & Eaton (2000).

3. Near-wall turbulence structures

Several types of structures were identified in the boundary layers. As mentioned above, low- and high-speed streaks and quasi-streamwise vortices are the dominant coherent structures in the near-wall region. These structures are closely related to the production of wall turbulence (Robinson 1991). In this section, our discussion focuses on the effects of the APGs on the near-wall streaky structures and quasi-streamwise vortices and on the APGs' statistical properties.

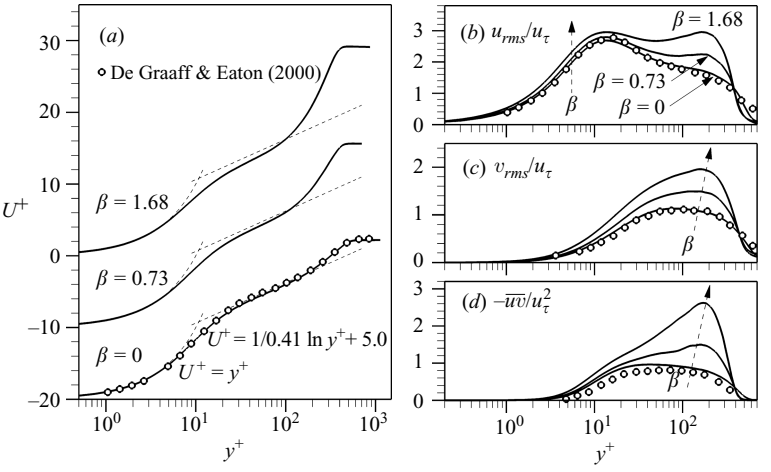

FIGURE 4. (*a*) Mean velocity profiles. Root-mean-square velocity fluctuations: (*b*) u_{rms}; (*c*) v_{rms}; (*d*) Reynolds shear stress.

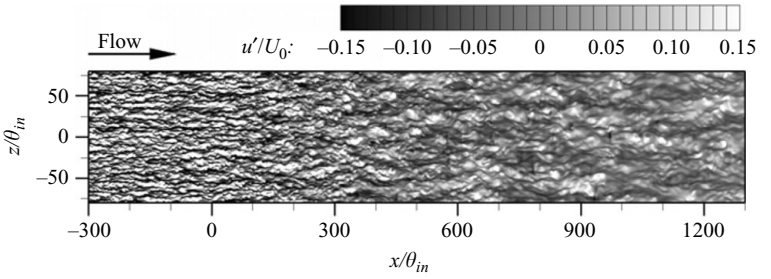

FIGURE 5. Instantaneous streamwise velocity fluctuation contours in a strong APG boundary layer ($m = -0.2$) at $y^+ = 5.5$ (at $x = 900\theta_{in}$).

3.1. *Instantaneous near-wall streaky structures*

To investigate the responses of near-wall streaky structures to APGs, we visualized the instantaneous streamwise velocity fluctuations for a strong APG TBL ($m = -0.2$). The streamwise velocity streaks in the x–z plane at $y^+ \approx 5.5$ are illustrated in figure 5. The contours are normalized by free-stream velocity at the inlet U_0. The dark and white areas represent lower- and higher-speed streaks respectively. The boundary layer develops under a ZPG at the inlet, and the streamwise pressure gradient becomes strongly adverse. Elongated streaks in the streamwise direction are clearly visible near the inlet. The spacing between the streaks is well established. As the TBL is subjected to the APG, the streaks are weakened compared with those in the inlet. A similar damping effect of an APG on such streaks was also found in the results of Skote & Henningson (2002).

The streaks are still visible in the APG region but are not as well-resolved as in the ZPG region (see figure 5). The velocity fields were normalized with root-mean-square velocity fluctuations in an attempt to visualize the near-wall streaks more clearly. The near-wall streaks in the ZPG region are presented in figure 6(*a*) for comparison. The field in figure 6(*b*) was obtained from the APG region identified in figure 5. The grey areas and solid-line contours correspond to low- and high-speed streaks respectively. The instantaneous characteristics of individual streaks in the APG and

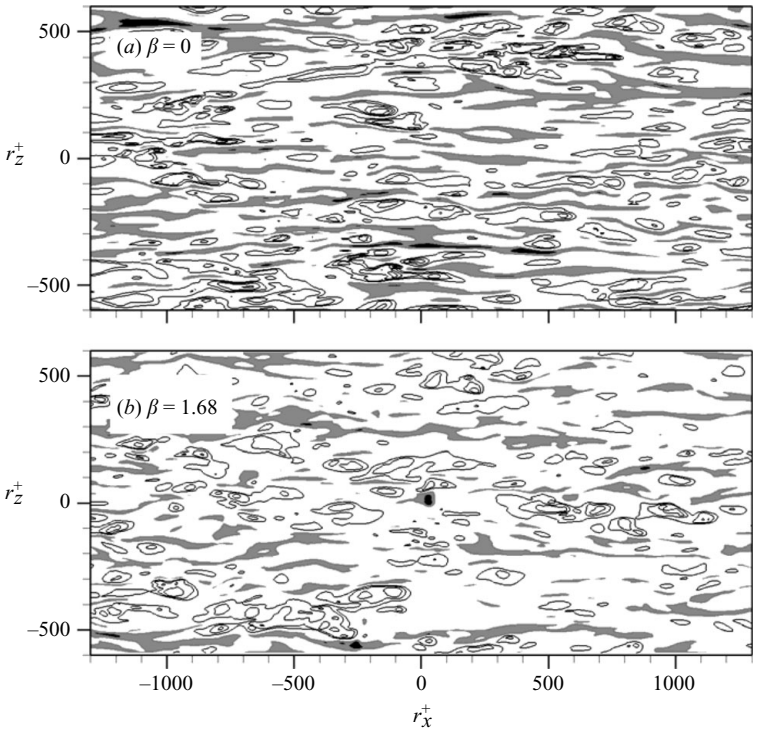

FIGURE 6. Streamwise velocity fluctuations at approximately $y^+ = 5.5$ (grey flooded area, $u' < -u_{rms}$; solid lines, $u' > -u_{rms}$): (*a*) $\beta = 0$; (*b*) $\beta = 1.68$. Contour levels are incremented by u_{rms}.

ZPG boundary layers are qualitatively very similar. The low-speed streaks are longer and narrower than the high-speed streaks in both flows. Similar observations were obtained by Robinson (1991) in a study of ZPG boundary layers. The widths of the low-speed streaks are also similar in the APG and ZPG flows. As can be seen in figure 6(*a*), the distance in the spanwise direction between the two streaks is well established and is approximately 100 viscous wall units for the ZPG flow (Smith & Metzler 1983). However, the spacing of the streaks is affected significantly by the strong APG. This result is inconsistent with that of the study of Finnicum & Hanratty (1988), who suggested that the streak spacing is insensitive to the pressure gradient, although strong effects were found for strong favourable gradient flows. In contrast, it is apparent from figure 6(*b*) that the spanwise spacing of the near-wall streaks is irregular and increases significantly up to 400 viscous wall units in the APG flow. Since instantaneous realizations cannot be used to define quantitative structural information unambiguously, a statistical analysis is necessary.

3.2. *Statistical analysis of near-wall streaks*

Two-point correlations were used to extract information about the size and relative locations of near-wall streaky structures quantitatively. The two-point correlation coefficients are defined as

$$R_{AB}(\boldsymbol{r}) = \frac{\langle A(\boldsymbol{x})B(\boldsymbol{x}+\boldsymbol{r})\rangle}{A_{rms}B_{rms}}, \tag{3.1}$$

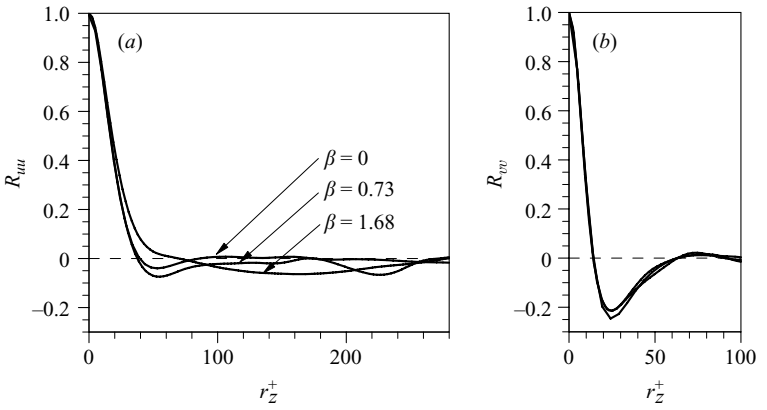

FIGURE 7. Spanwise two-point correlations at $y^+ = 5.5$: (*a*) R_{uu}; (*b*) R_{vv}.

where $\boldsymbol{r}$ denotes the spatial separation vector and A_{rms} and B_{rms} are the root mean squares of A and B respectively. The auto-correlation R_{uu} of the streamwise velocity has previously been used to study the properties of such streaks (Kim, Moin & Moser 1987). Figure 7(*a*) shows the auto-correlation R_{uu} as a function of spanwise spatial separation. The results for the APG and ZPG flows appear to coincide at $R_{uu} > 0.2$. This result confirms statistically that the widths of the individual streaks are less sensitive to the APG. Kim *et al.* (1987) suggested that the average spanwise spacing between the streaks is roughly twice the separation between the minima in R_{uu}. The correlations become negative and reach a minimum at $r_z^+ \approx 50$, except when $\beta = 1.68$. In particular, the negative peak in the correlations for $\beta = 1.68$ is broad and is located at a larger separation in the range $80 < r_z^+ < 240$. These statistical results indicate that the near-wall streaks are dominant in the strong APG boundary layer and that the strongest APG considered here does not affect the individual widths of the streaks. However, the spanwise spacing of the streaks is increased and disordered by the strong APG. The conditional correlations are considered to investigate the effect of the APG on the streamwise extent of near-wall low- and high-speed streaks. The conditional correlations are defined as

$$\left.\begin{aligned} R_{uu}(\boldsymbol{r}|u(\boldsymbol{x}) < 0) &= \frac{\langle u(\boldsymbol{x})u(\boldsymbol{x}+\boldsymbol{r})|u(\boldsymbol{x}) < 0\rangle}{\langle u(\boldsymbol{x})u(\boldsymbol{x})|u(\boldsymbol{x}) < 0\rangle}, \quad \text{for low-speed streak,} \\ R_{uu}(\boldsymbol{r}|u(\boldsymbol{x}) > 0) &= \frac{\langle u(\boldsymbol{x})u(\boldsymbol{x}+\boldsymbol{r})|u(\boldsymbol{x}) > 0\rangle}{\langle u(\boldsymbol{x})u(\boldsymbol{x})|u(\boldsymbol{x}) > 0\rangle}, \quad \text{for high-speed streak.} \end{aligned}\right\} \tag{3.2}$$

The resulting two-dimensional conditional correlations associated with low- and high-speed streaks are shown in figure 8. The average streamwise dimension of the low-speed streak for $\beta = 0$ (ZPG) is longer than that for $\beta = 1.68$ (APG). For $\beta = 0$, the 0.15 contours show that the average streamwise extent of the structure exceeds 1000 viscous wall units. For $\beta = 1.68$, the average length is approximately 700 viscous wall units. The low-speed streaks are longer than the high-speed streaks in both flows. These results are consistent with the instantaneous realizations in figure 6.

3.3. *Instantaneous visualization of near-wall vortical structures*

Figure 9 shows the instantaneous vortical structures in the near-wall region. We adopted the vortex identification method of Zhou *et al.* (1999) to visualize the near-wall vortices. They identified vortices by using an isosurface of swirling strength λ_{ci}, where λ_{ci} is the imaginary part of the complex eigenvalue of the velocity gradient

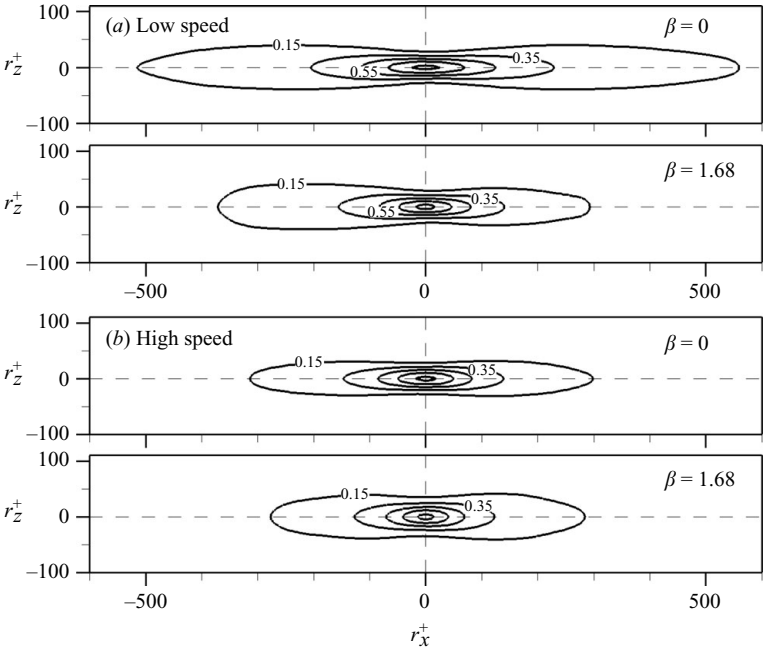

FIGURE 8. Conditional two-point correlation coefficients of the streamwise velocity fluctuations at $y^+ = 5.5$. The specified events are (*a*) $u < 0$ and (*b*) $u > 0$. Contour levels are from 0.15 to 0.95 with increments of 0.2.

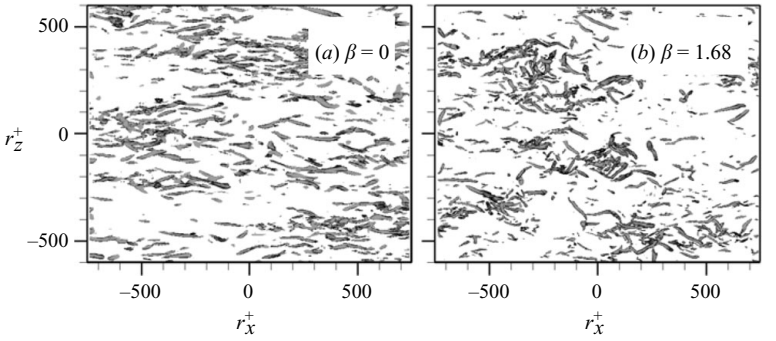

FIGURE 9. Near-wall vortical structures ($y^+ < 50$): (*a*) $\beta = 0$; (*b*) $\beta = 1.68$.

tensor. The swirling strength is a quantity used to detect vortex cores and to distinguish vortical structures from shear regions. Isosurface values of 20 % of maximum were used for both the APG and ZPG flows. The near-wall vortical structures survive even in the presence of a strong APG. Quasi-streamwise vortices are still dominant in the near-wall region in the presence of the APG and can be identified as much as for the ZPG flow. One difference between the APG and ZPG flows is that vortical structures are more inclined in the spanwise direction at $y^+ < 50$ in the APG boundary layer.

The auto-correlation R_{vv} as a function of spanwise spatial separation is shown in figure 7(*b*). The auto-correlation R_{vv} of the wall-normal velocity can be used to study the properties of quasi-streamwise vortices (Kim *et al.* 1987). The separation of the minima in R_{vv} corresponds to the average radius of the streamwise vortices. The separation of the minima in R_{vv} at $r_z^+ \approx 25$ remains unchanged as β varies and

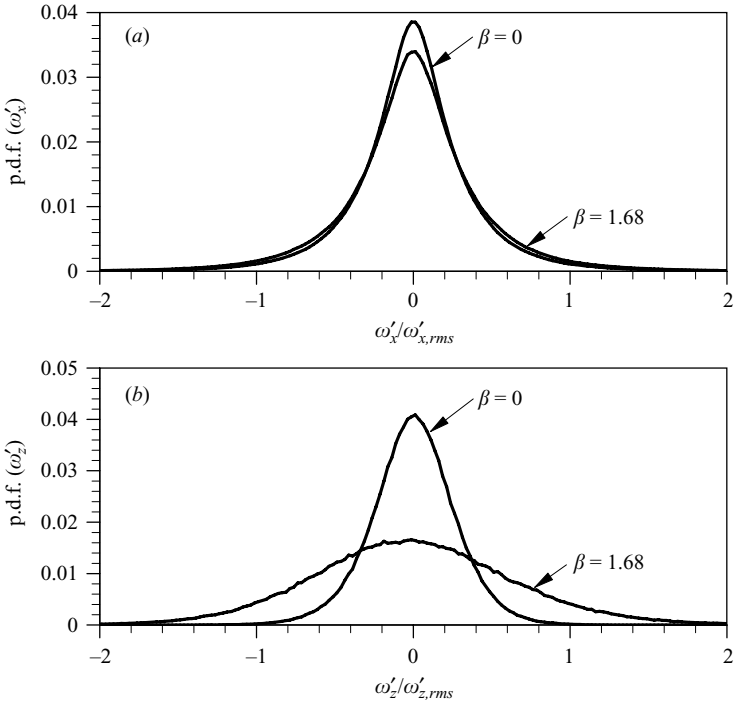

FIGURE 10. Distributions of the p.d.f. for (*a*) streamwise vorticity fluctuations and (*b*) spanwise vorticity fluctuations at approximately $y^+ = 20$.

is similar to that for the ZPG flow. The average diameter of 50 viscous wall units is probably insensitive to the strength of the APG. The probability density functions (p.d.f.s) were calculated to compare the APG and ZPG flows statistically. The p.d.f.s for the streamwise vorticity fluctuations ω_x at $y^+ \approx 20$ are depicted in figure 10(*a*). In this figure, the vorticity fluctuations are normalized by their root-mean-square values. The APG and ZPG results are in good agreement except near $\omega_x' = 0$, which indicates that the streamwise vortices are nearly identically distributed in the ZPG and APG flows. Figure 10(*b*) shows the p.d.f.s of the spanwise vorticity fluctuations. It is clear that strong fluctuations ($|\omega_z'| > 0.5\,\omega_{z,rms}$) occur more frequently in the APG flow than in the ZPG flow. This result indicates that quasi-spanwise vortices are more activated in the APG flows and is consistent with the instantaneous realizations shown in figure 9.

3.4. *Conditional events*

Vortical structures are closely related to the production of Reynolds shear stress (Robinson 1991). Moin, Adrian & Kim (1987) proposed that conditionally averaged vortical structures can be identified by carrying out an LSE based on the velocity vector that makes the largest contribution to the Reynolds shear stress. We examined the near-wall vortical structures associated with the production of Reynolds shear stress by using the method of Moin *et al.* (1987). The weighted joint p.d.f.s, $u'v'p.d.f.(u', v')$, were examined to determine the conditional event vector $\boldsymbol{u}_E = (u_m, v_m)$. These events were detected by finding the maximum values of $u'v'p.d.f.(u', v')$ in the second and fourth quadrants (Q2 and Q4). These Q2 and Q4 events contribute to the positive production of Reynolds shear stress. The event

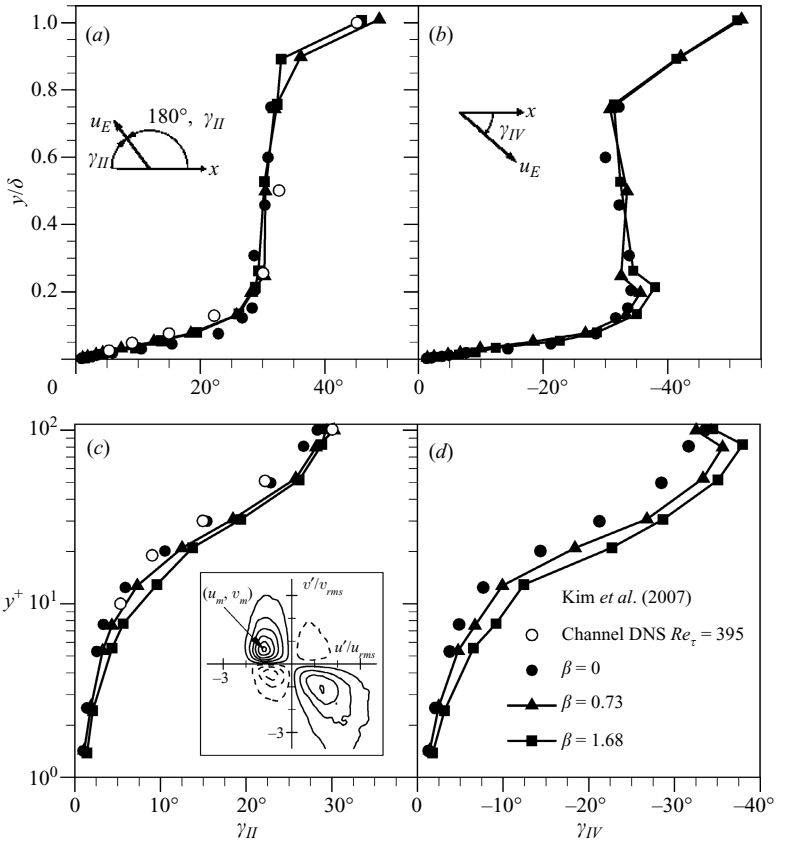

FIGURE 11. Angle of the velocity vector with the maximum contribution to the Reynolds shear stress. In outer units: (*a*) the Q2 event vector; (*b*) the Q4 event vector. In inner units: (*c*) the Q2 event vector; the Q4 event vector. The inset shows an example of contours of probability weighted Reynolds shear stress $u'v'\,p.d.f.(u', v')$ at $y^+ = 5.5$ for $\beta = 1.68$.

angles $\gamma = \tan^{-1}(v_m/u_m)$ defined by $\boldsymbol{u}_E$ are presented in figure 11 for all three values of β. Note that the flow structures estimated with the same v_m/u_m have the same shapes (Moin *et al.* 1987).

Figures 11(*a*) and 11(*c*) show the Q2 event angles (γ_{II}) as functions of y normalized by the outer and inner variables respectively. For comparison, the results for channel flow at $Re_\tau = 395$ from Kim, Sung & Adrian (2008) are also included. The profile of the ZPG boundary layer is in good agreement with that for channel flow. This result suggests that the angle of the velocity vector with the largest contribution to the Reynolds shear stress is independent of flow type, i.e. channel flow or boundary layer. As shown in figure 11(*c*), γ_{II} grows with y for fixed β at $y^+ < 100$. The rapid change near $y^+ = 30$ is attributed to a change in the dominant structure, from quasi-streamwise vortices to hairpin vortices inclined with respect to the flow (Moin *et al.* 1987). The APG Q2 event vectors have larger inclination angles than those for the ZPG flow: as β increases, γ_{II} increases. The increase in γ_{II} with β is partly due to the frequent appearance of transverse structures, which induce ejection motions inclined at a deeper angle than those of the streamwise vortices in the near-wall region, as shown in figure 9.

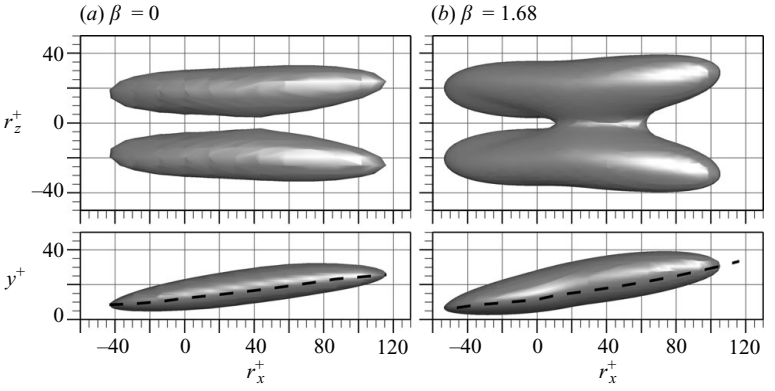

FIGURE 12. Vortical structures of the linearly estimated velocity field for the Q2 event vector, $u_E = (u_m, v_m, 0)$ at $y^+ = 5.5$. Also plotted is the loci of the maximum swirling strength.

The behaviour of the Q4 event angle (γ_{IV}) in the near-wall region is similar to that observed for γ_{II}; γ_{IV} grows with y for fixed β and increases with increasing β, as can be seen in figure 11(d). An obvious difference between the APG and ZPG flows is that in the former systems a new peak forms at the log layer as β increases. This peak is attributed to the effect of large-scale sweep motions in this region. The downward diffusion of turbulence has been observed in many previous studies of strong APG TBLs (Nagano *et al.* 1993; Krogstad & Skåre 1995; Houra, Tsuji & Nagano 2000; Lee & Sung 2008). The predominant downward motions with large inclination angles with respect to the flow contribute significantly to Reynolds shear stress in the log region of the APG TBLs. Outside the log layer in figures 11(a) and 11(b), the inclination angle is roughly constant at approximately 30° up to $y/\delta = 0.6$, where δ is the boundary layer thickness, beyond which it increases. The inclination angle is roughly insensitive to the strength of the APG in this region.

3.5. *Linear estimation of near-wall vortical structures*

Conditional eddies around the Q2 events that make the largest contribution to the mean Reynolds shear stress of APG and ZPG at $y^+ \approx 5.5$ are compared in figure 12. We employed LSE because direct computation of the conditional averages is impractical. It is well known that LSE is a robust conditionally averaged approximation that provides satisfactory results for various turbulent fields (Adrian *et al.* 1989). A stochastic estimate of a conditionally averaged flow field can be obtained by expanding the conditional average in a power series about the event E_j, i.e.

$$\langle u_i | E_j \rangle = L_{ij} E_j + M_{ijk} E_j E_k + L. \tag{3.3}$$

The unknown coefficients $L_{ij}, M_{ijk}, \ldots$ can be determined by minimizing the mean-square error between the approximation and the conditional average. In the case of linear estimation, only the first term is retained and the minimization yields

$$\langle E_j(x) E_k(x) \rangle L_{ij} = \langle u_i(x + r) E_k(x) \rangle. \tag{3.4}$$

From (3.4), the linear estimate of the conditional average $\hat{u}_i(x + r)$ of $\langle u_i(x + r) | u_m(x), v_m(x) \rangle$ reduces to

$$\hat{u}_i(x + r) = L_{i1} u_m(x) + L_{i2} v_m(x), \tag{3.5}$$

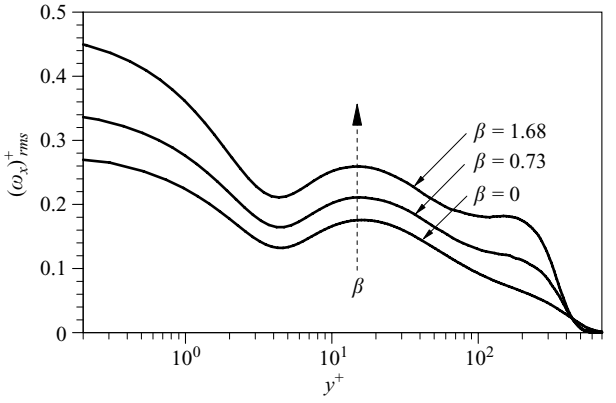

FIGURE 13. Root-mean-square streamwise vorticity fluctuations in wall coordinates.

with $i = 1$, 2 and 3 and

$$\begin{bmatrix} L_{i1} \\ L_{i2} \end{bmatrix} = \frac{1}{u_{rms}^2 v_{rms}^2 - \langle uv \rangle^2} \begin{bmatrix} v_{rms}^2 & -\langle uv \rangle \\ -\langle uv \rangle & u_{rms}^2 \end{bmatrix} \begin{bmatrix} \langle u(x)u_i(x+r) \rangle \\ \langle v(x)u_i(x+r) \rangle \end{bmatrix}. \tag{3.6}$$

The conditional eddies were visualized by using an isosurface of λ_{ci} based on the conditionally averaged velocity fluctuation fields. The conditional eddy for the given Q2 event takes the form of a quasi-streamwise vortex with its centre located near $y^+ = 20$. This geometry is consistent with the instantaneous fields. The streamwise vortices are out of phase in reality (Jeong *et al.* 1997). The symmetrical shape of conditional averaging is due to the statistical symmetry of the given event with respect to the reflection about the vertical plane at $r_z^+ = 0$.

The inclination angle in the vertical plane is about 7° for the ZPG flow. The inclination angle was evaluated from the loci of the maximum λ_{ci} inside the conditional eddies. This angle is slightly less than that reported by Jeong *et al.* (1997) for near-wall coherent structures. We expect such angles to be contaminated by near-wall streaks, since the LSE is based on two-point correlations that reflect information about the near-wall streaks (Hutchins, Hambleton & Marusic 2005). In the APG flow, the inclination angle of the streamwise vortex is slightly higher, approximately 9°. The educed vortices with an isosurface of $\lambda_{ci}\nu/u_t^2 = 0.017$ have streamwise extents of about 140 viscous wall units for both the APG and ZPG flows. However, the APG transverse and vertical extents are larger than those of the ZPG flow. This result indicates that the swirling motion in the APG streamwise direction is stronger than that in the ZPG flow. Although the distributions of near-wall vortices in the APG flows are similar to that in the ZPG flow, the enhanced swirling motion of the individual vortices in the presence of the APG results in an increase in the averaged vorticity fluctuations normalized by wall units in the near-wall region, as shown in figure 13.

4. Large-scale structures in the outer region

Various results indicating the presence of LMRs and packets of hairpin vortices in ZPG flows have recently been reported (Adrian *et al.* 2000; Ganapathisubramani *et al.* 2003). Although several types of structures are present in the outer layers of TBLs, it appears that elongated LMRs and hairpin packets are the dominant outer

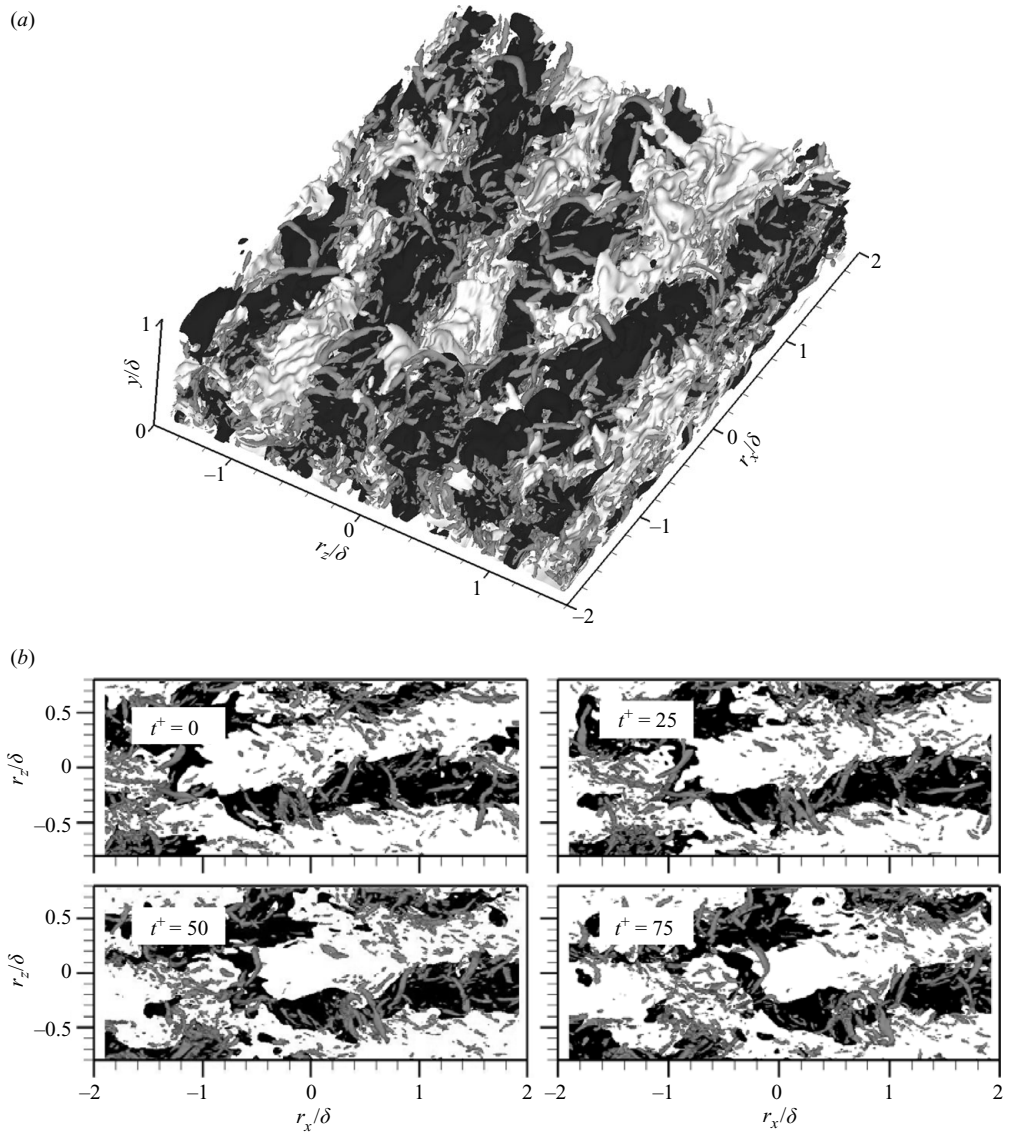

FIGURE 14. Outer vortical structures in an APG boundary layer ($\beta = 1.68$): (*a*) perspective view; (*b*) top view. The vortices are shown as grey isosurface plots of swirling strength (11 % of maximum λ_{ci}). The black and white areas are low- and high-speed regions (10 % below and above local free-stream velocity) respectively.

layer structures associated with turbulence production (Ganapathisubramani *et al.* 2003). LMRs and coherent groups of vortices are also present throughout the outer layers of the APG flows. Figure 14 shows a visualization of an instantaneous flow field subjected to a strong APG. Several elongated low-speed regions are present in the outer layer, and each of them lies beneath a group of streamwise-aligned hairpin-like structures. Snapshots of time evolution indicate that the group of vortices convects downstream with coherence. In this section, we discuss these large-scale structures in the outer layers of APG TBLs and their statistical properties.

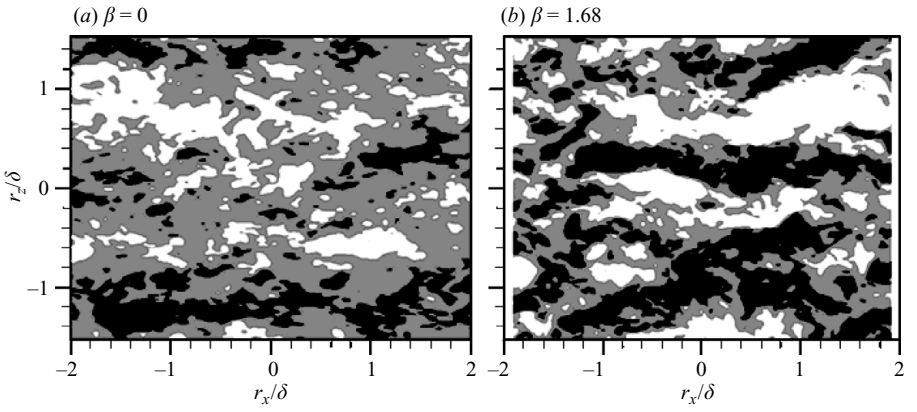

FIGURE 15. Instantaneous u-velocity contours at $y/\delta = 0.2$: (*a*) $\beta = 0$; (*b*) $\beta = 1.68$. The black and white areas represent regions with velocities 10 % below and above local mean velocity respectively.

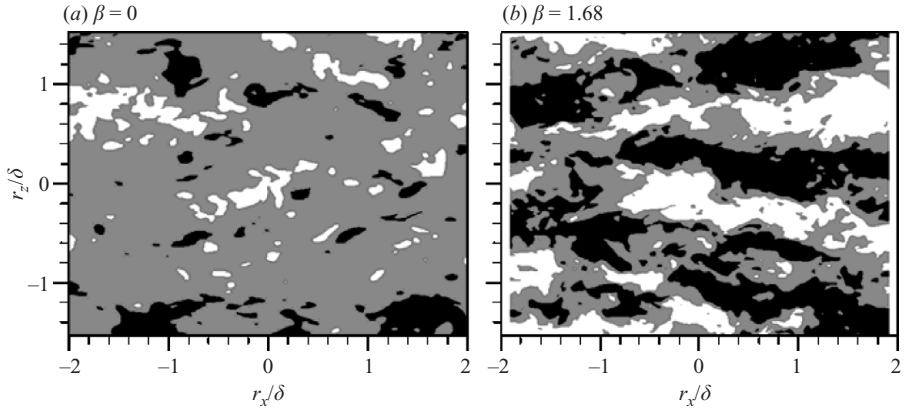

FIGURE 16. Instantaneous u-velocity contours at $y/\delta = 0.45$: (*a*) $\beta = 0$; (*b*) $\beta = 1.68$. The black and white areas represent regions 10 % below and above the local mean velocity respectively.

4.1. *Instantaneous visualizations of large-scale outer structures*

Flow visualizations were performed to demonstrate the presence of LMRs in the outer layers of APG TBLs. Figure 15 shows the streamwise velocity contours in the x–z plane at the top of the log layer. The white and black areas correspond to higher- and lower-speed fluid regions respectively. LMRs are also present in the APG flow and are highly elongated in the streamwise direction, as described for ZPG boundary layers by Tomkins & Adrian (2003). In both realizations, there are three LMRs in the log layer. Each LMR extends beyond the streamwise range examined, indicating the presence of streamwise regions longer than 4δ. The width of the LMRs is about 0.4δ.

Figure 16 shows LMRs in the wake region at the same representative time under consideration in figure 15. In the ZPG flow, fewer LMRs are visible at $y/\delta = 0.45$. This result is consistent with the experimental observation that low-speed regions in the wake region of a ZPG TBL are difficult to identify because the larger packets in this region induce weaker low-speed flow (Adrian *et al.* 2000). In the APG flow, however, the LMRs in the wake region are similar to those at the top of the log

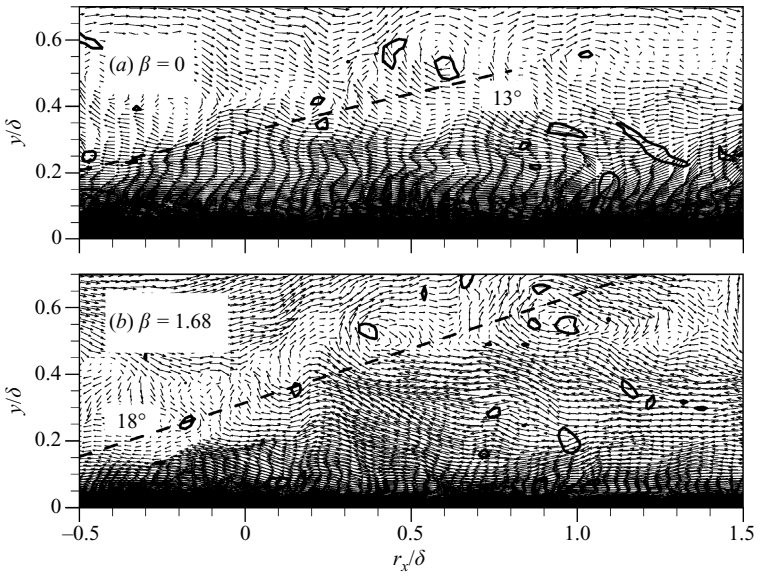

FIGURE 17. Instantaneous velocity vector fields with the constant convection velocity removed: (*a*) $\beta = 0$; (*b*) $\beta = 1.68$. Contours of λ_{ci} are shown in the background to highlight the location of the vortex cores.

layer in figure 15(*b*); i.e. they are still dominant and regular in the wake region. These findings support the conclusion that the outer LMRs are intensified and regulated by the APG and that strong velocity fluctuations with respect to the mean velocity are present in the outer streaky structures. We suggest that the outer maximum peaks observed in the Reynolds stress profiles and in the turbulence intensities of APG TBLs (figures 8 and 9 of Lee & Sung 2008) are related to the outer streaky structures.

Galilean decomposition has been used to detect swirling motions in flows. If the convection velocity is subtracted from the flow field, velocity vectors with a streamwise component that is similar to the selected convection velocity have a small magnitude, so such regions appear light in the visualization. Vortex patterns moving with a velocity equal to the subtracted convection velocity are seen in such light regions. Figure 17 shows the instantaneous velocity fields in the streamwise–wall-normal plane of the boundary layer for the ZPG and APG flows. The velocity fields were processed with the Galilean frames. The swirling strength contours are also shown in the background to highlight the locations of the vortex cores. A single vortex packet is evident in both flows. In the APG flow, several vortex cores are aligned with an inclination angle of about 18° relative to the wall and advect with a similar convection velocity. These vortex cores are associated with the heads of hairpin-like vortices, i.e. asymmetric hairpins, cane-like vortices, horseshoe vortices or hairpin vortices. The ejection of low-speed fluid away from the wall under the vortex is consistent with the hairpin vortex signature introduced by Adrian *et al.* (2000). The inclination angle of the packet in the APG flow is larger than that for the ZPG flow, for which the angle is approximately 13°. However, these large-scale structures are similar to those proposed in the conceptual model of hairpin packets in ZPG TBLs of Adrian *et al.* (2000). These instantaneous fields indicate that vortex packets are common features in the outer regions of TBLs subjected to an APG.

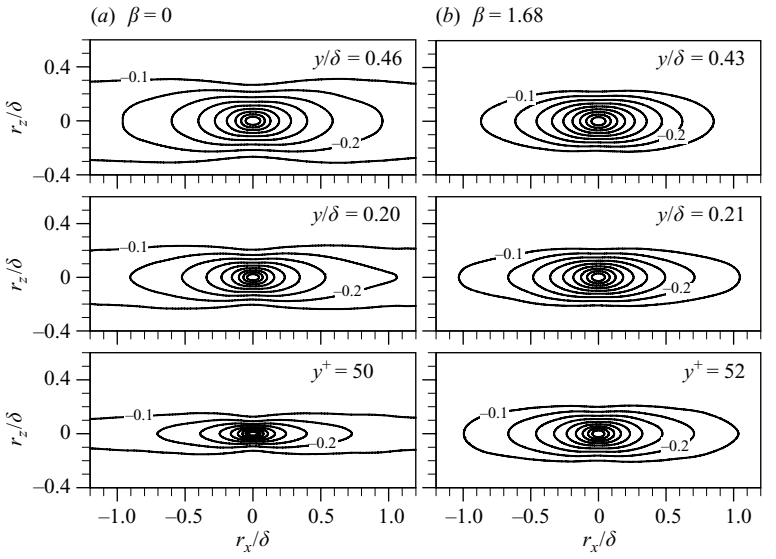

FIGURE 18. Given a negative-u event, u-contours of the linear estimate: (a) $\beta = 0$; (b) $\beta = 1.68$.

4.2. *Linear estimation of LMRs*

The instantaneous realizations presented in the preceding section demonstrate the presence and dominance of LMRs in the outer layers of APG TBLs. In this section, LSE is employed to obtain quantitative structural information about the LMRs in TBLs subjected to APGs. LSE has previously been used to estimate the effects on a conditionally averaged velocity field on the presence of a negative streamwise velocity event (Adrian & Moin 1988). Tomkins & Adrian (2003) suggested that the average size of LMRs can be quantified from an LSE of conditionally averaged structures resulting from an event of negative fluctuating streamwise velocity. The linear estimate of the conditional average is given by

$$\hat{u}_i(x + r) = L_{i1} u_1(x), \tag{4.1}$$

with $i = 1$, 2 and 3 and

$$L_{i1} = \frac{\langle u_i(x + r) u_1(x) \rangle}{\langle u_1^2 \rangle}. \tag{4.2}$$

Estimates were obtained at the log layer and in the middle of the boundary layer. The velocity contours of the estimates in figure 18 show that the conditionally averaged structure is a large low-speed region that is elongated in the streamwise direction. This result is in good agreement with the instantaneous fields. These LSE results provide statistical support for the conclusion that LMRs are the dominant structure in the outer regions of APG TBLs. The average length and width of these structures were quantified from the streamwise velocity contours. Since the streamwise extent of low contours such as -0.1 is beyond the streamwise view of this data and is not reliable, higher-level contours were used to estimate the average properties of the conditional structure. Figures 19(a) and 19(b) illustrate the length and width scales respectively of the conditionally averaged structure based on the extent of the -0.4 contour, as a function of y/δ. The length scale L increases linearly with y in the log layer ($y^+ > 30$, $y/\delta < 0.2$) for both the APG and ZPG flows. The streamwise lengths

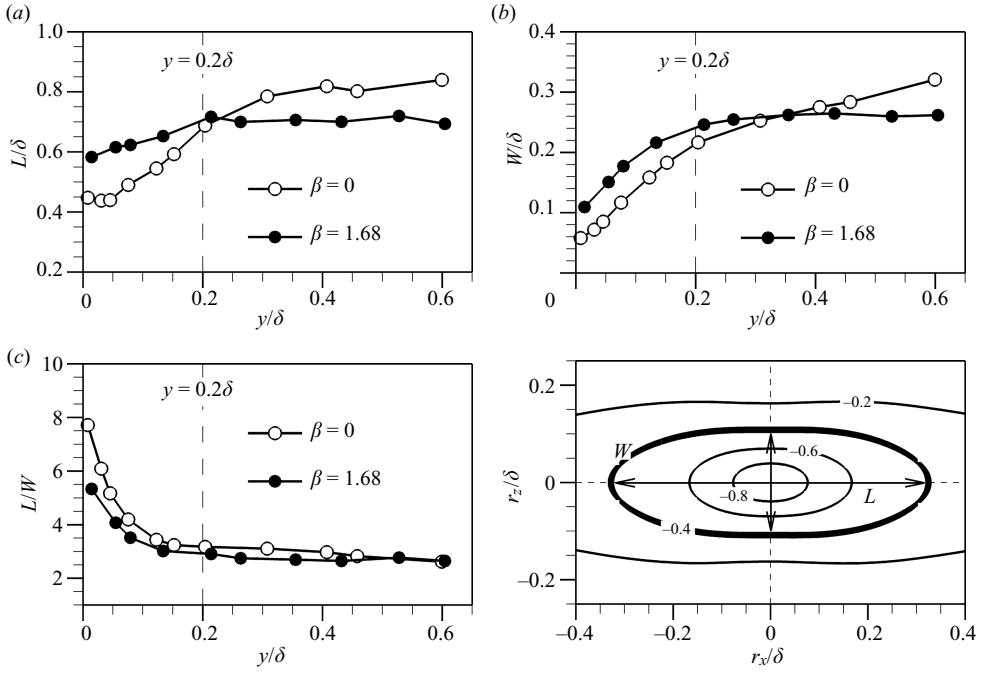

FIGURE 19. (*a*) Streamwise and (*b*) spanwise extent of the −0.4 contour of conditional *u*-velocity. (*c*) Aspect ratio of the streamwise to spanwise extents, L/W.

normalized by δ of the structures of the APG flow are larger than those of the ZPG flow in this region. The difference between the APG and ZPG lengths is largest at the bottom of the log layer and decreases with distance from the wall.

Figure 19(*b*) shows that the average spanwise width W grows almost linearly with distance from the wall in the log region. The linear variation of the spanwise scales with y is consistent with Townsend's attached-eddy hypothesis. Although the widths normalized by δ of the APG flow are larger than those of the ZPG flow, the rate of growth of the width in the near-wall region is similar for both flows. Figure 19(*c*) shows the ratio L/W as a function of the wall-normal location y/δ. The APG ratio lies between 5.3 and 2.3. The APG ratio is generally less than that of the ZPG flow, i.e. between 7.7 and 2.4. This result indicates that the LMRs of the APG flow are less elongated than those of the ZPG flow due to the influence of the APG. The difference between the APG and ZPG L/W ratios is largest near the wall and decreases rapidly with increase in the distance from the wall.

Beyond the log layer, the length scale of the APG flow is approximately constant up to $y/\delta = 0.6$. In contrast, the length scale of the ZPG flow increases slightly. The width scale exhibits a trend similar to that of the length scale. In their study with correlation-based length measurements of TBLs near separation, Krogstad & Skåre (1995) reached a similar conclusion. As a result, the aspect ratio remains roughly constant at 2.7 in this region, $0.2 < y/\delta < 0.6$. These results support the conclusion that well-organized LMRs appear in the wake regions of APG TBLs more regularly than in those of ZPG TBLs, as shown in figure 16. As a consequence, the average shape of the LMRs in the x–z plane seems to be statistically identical throughout the wake region ($0.2 < y/\delta < 0.6$).

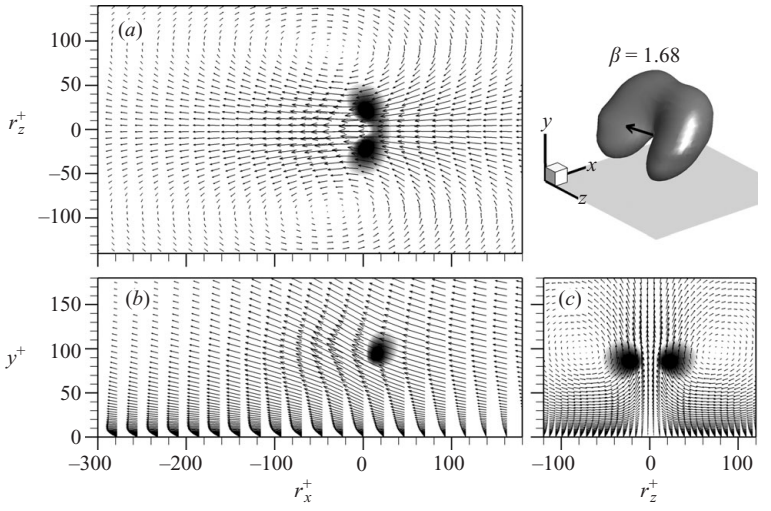

FIGURE 20. Linearly estimated velocity vector fields with the Q2 event at $y^+ = 83$ on the (*a*) *x*–*z*, (*b*) *x*–*y* and (*c*) *y*–*z* planes at $y^+ = 83$, $r_z^+ = 0$ and $r_x^+ = 0$, respectively. Flooded contours of λ_{ci} are shown in the background to indicate the locations of the vortices.

4.3. *Conditional eddies*

Previous experimental and numerical studies have shown that the Reynolds shear stress increases in the outer region of the boundary layer and that the maximum peak moves away from the wall (Skåre & Krogstad 1994; Lee & Sung 2008). As mentioned above, the vortex structures are responsible for the production of Reynolds stress. We investigated the changes in the vortical structures in the outer region as the Reynolds shear stress increases. LSE was employed following the same method as used in § 3.5 to obtain the conditionally averaged vortical structures associated with the Reynolds stress. Figure 20 shows an example of the conditionally averaged velocity fields associated with the dominant Q2 event in the logarithmic region of an APG TBL. The velocity vectors are plotted with the mean velocity subtracted. The conditional eddy was found to be a hairpin-like vortex. This geometry is qualitatively similar to the conditionally averaged vortical structure found in the turbulent channel data of Zhou *et al.* (1999). The vortex is identified in a three-dimensional perspective with an isosurface of $\lambda_{ci}\nu/u_t^2 = 0.022$. The flooded swirling strength contours in these vector plots clarify the locations of the vortical structures. The induced upward motion of the low-speed fluid between the two legs of the structure is clear in these vector plots. The velocity vectors indicate that there are counter-rotating vortical motions around the vortex legs in the *y*–*z* plane at $r_x^+ = 0$. In the *x*–*z* plane at the *y*-location of the given conditional event, the vortex is located on the LMR. These results suggest that hairpin-type vortices are the predominant structures associated with the production of Reynolds stress in the APG flows and that they are related to LMRs.

The isosurfaces of λ_{ci} for the vortical structures of the linearly estimated velocity fields of the Q2 event at $y^+ = 50$ and $y/\delta = 0.45$ are illustrated in figures 21 and 22 respectively. For the conditional eddies associated with the Q2 event at the bottom of the logarithmic region, the streamwise lengths of the eddies in the APG flow are similar to those of the ZPG flow identified by $\lambda_{ci}\nu/u_t^2 = 0.028$. However, the legs of the hairpin increase in size as β increases. The inclination angle of the vortex leg also increases with increasing β. For the conditional eddies associated with the Q2 event at

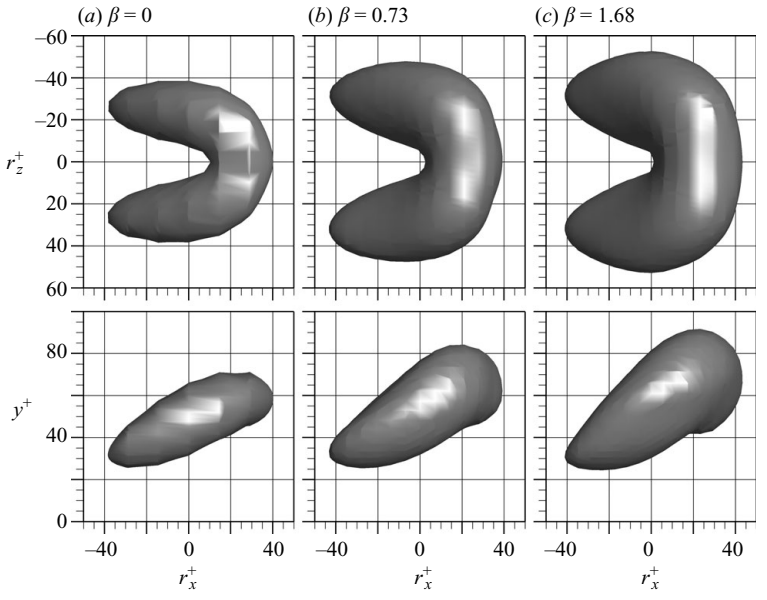

FIGURE 21. Vortical structures of the linearly estimated flow field for the Q2 event vector, $u_E = (u_m, v_m, 0)$, at approximately $y^+ = 50$.

$y/\delta = 0.45$, the spanwise extents of the eddies in the APG flow are larger than those in the ZPG flow detected by an isosurface of swirling strength (60 % of maximum λ_{ci}). The difference between the APG and ZPG eddy sizes increases when the eddies are identified by the same isosurfaces, i.e. $\lambda_{ci}\delta/U_\infty = 0.25$. This result implies that the swirling motion of the individual vortex located in the wake region of the APG flow is stronger than that of the ZPG flow and thus supports the observations for instantaneous realizations of outer vortices of Lee & Sung (2008).

The loci of maximum swirling strength inside the conditional eddies are illustrated in figure 22 to further characterize the size and shape of the eddies. Figure 23(a) shows that the cores of the conditional structures associated with the Q2 event at $y^+ = 50$ take the form of a hairpin-like eddy with two quasi-streamwise vortices. The centres of the upstream streamwise vortices are located near $y^+ = 20$ and 83 viscous wall units apart in the spanwise direction for $\beta = 1.68$. This separation is slightly larger than that of the ZPG flow ($\beta = 0$), i.e. 68 viscous wall units. The vortices have shallow inclination angles in the vertical plane of 9.2° and 8.8° for the APG and ZPG flows respectively. These angles are similar to the inclination angle of the near-wall streamwise vortex described in § 3.5. The downstream part of the hairpin legs of about 60 viscous wall units for $\beta = 1.68$ has a steeper inclination angle of 28.8°. This angle is higher than the angle in the ZPG flow (21.3°). The steeply inclined part of the conditional eddies associated with the Q2 event at $y/\delta > 0.2$ resembles a Λ shape. In this part, the spanwise spacing between the centre of each vortex leg decreases almost linearly with distance from the wall, as shown in figures 23(b) and 23(c). The inclination angle in the x–z plane is about 32.8° for the y-location of the conditional event at $y/\delta = 0.45$. Note that there is a strong similarity between the Λ-shaped parts of the conditional eddies for the given events at the same wall-normal location for the APG and ZPG flows, when the length scales are normalized by δ. The inclination

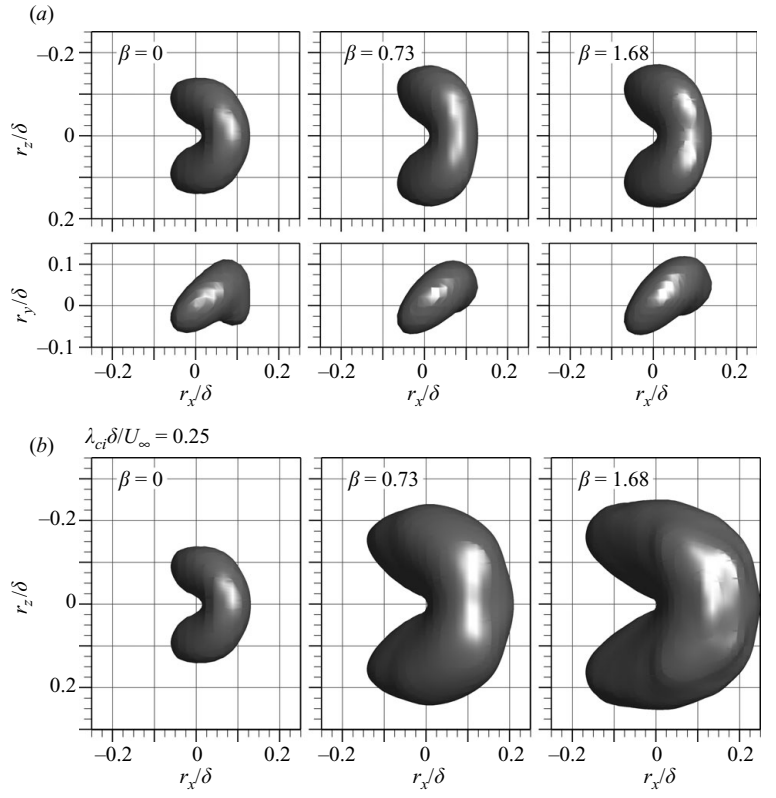

FIGURE 22. Vortical structures of the linearly estimated flow field for the Q2 event vector, $u_E = (u_m, v_m, 0)$, at $y/\delta \approx 0.45$: (*a*) isosurface of 60 % of maximum λ_{ci}; (*b*) isosurface of $\lambda_{ci}\delta/U_\infty = 0.25$.

angle of the vortex leg of approximately 30° in the vertical plane is similar for the APG and ZPG flows (figure 24*e*).

Figures 24(*a*)–24(*c*) show the loci of the eddy centres at $r_x/\delta = 0$, -0.1 and -0.15 respectively for all conditional eddies. The spanwise spacing between the vortex cores increases with distance from the wall in the log region. Beyond the log region, the spanwise spacing is approximately constant for both the APG and ZPG flows. The spanwise separations at the upstream ends of the eddies are about 0.4δ, as shown in figure 23(*c*). This result is in good agreement with the width of the LMRs estimated above from the instantaneous realizations. This result supports the idea that the hairpin-like eddies grow or merge with each other in the log layer, as suggested by Tomkins & Adrian (2003), and mature beyond the log layer to a width similar to that of the LMR at the corresponding distance from the wall. The ratio of the spanwise spacing between the vortex cores at $r_x/\delta = -0.1$ to the width of the LMR based on the -0.4 contours of LSE is plotted as a function of y/δ in figure 24(*d*). This ratio is roughly constant at approximately 1 in the outer region ($y/\delta > 0.2$) for both the APG and ZPG flows, although there is some scatter in the ratio. The width of the LMR is closely associated with the size of the individual conditional eddies in the outer region.

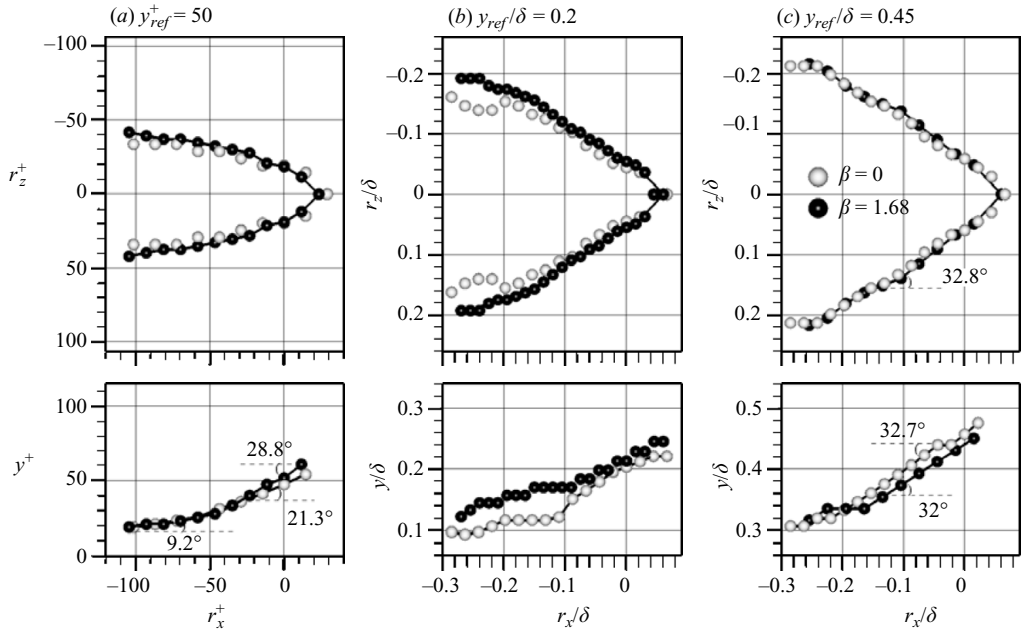

FIGURE 23. Loci of maximum swirling strength inside the conditional eddies for the Q2 event given at (*a*) $y^+ = 50$, (*b*) $y/\delta = 0.2$ and (*c*) $y/\delta = 0.45$.

4.4. *Stochastic estimation of vortex organization in the outer layer*

The above visualizations of instantaneous structures and velocity fields show that hairpin-like vortex organizations are associated with LMRs and are commonly visible in the outer regions of APG TBLs. In this section, we provide statistical evidence that the outer layers of APG TBLs are populated by organizations of vortices aligned coherently in the streamwise direction. To investigate the vortex organizations statistically, we now consider the LSE of the average flow field associated with a single spanwise vortical motion (represented by λ_{ci}). The analysis in this section follows that of Christensen & Adrian (2001). However, their approach to planar PIV data is extended for volumetric DNS data to educe the three-dimensional form of the vortex organization. Here λ_{ci} is calculated from the two-dimensional velocity gradient tensor $\boldsymbol{D}$ in the x–y plane, in order to detect only spanwise swirling motion at a given location if possible; $\boldsymbol{D}$ can be expressed as

$$\boldsymbol{D} = \begin{bmatrix} \partial u/\partial x & \partial u/\partial y \\ \partial v/\partial x & \partial v/\partial y \end{bmatrix}. \tag{4.3}$$

The conditional event is chosen to be a positive λ_{ci}. The LSE $\hat{u}_i(x + r)$ of this conditional average $\langle u_i(x+r)|\lambda_{ci}(x)\rangle$ is given by (Christensen & Adrian 2001)

$$\hat{u}_i(x + r) = L_i \lambda_{ci}(x), \tag{4.4}$$

with $i = 1$, 2 and 3 and

$$L_i = \frac{\langle \lambda_{ci}(x) u_i(x + r)\rangle}{\langle \lambda_{ci}(x)^2\rangle}. \tag{4.5}$$

It can be seen from (4.3) that two-point correlations between the swirling strength and the velocity are necessary to calculate the coefficient L_i.

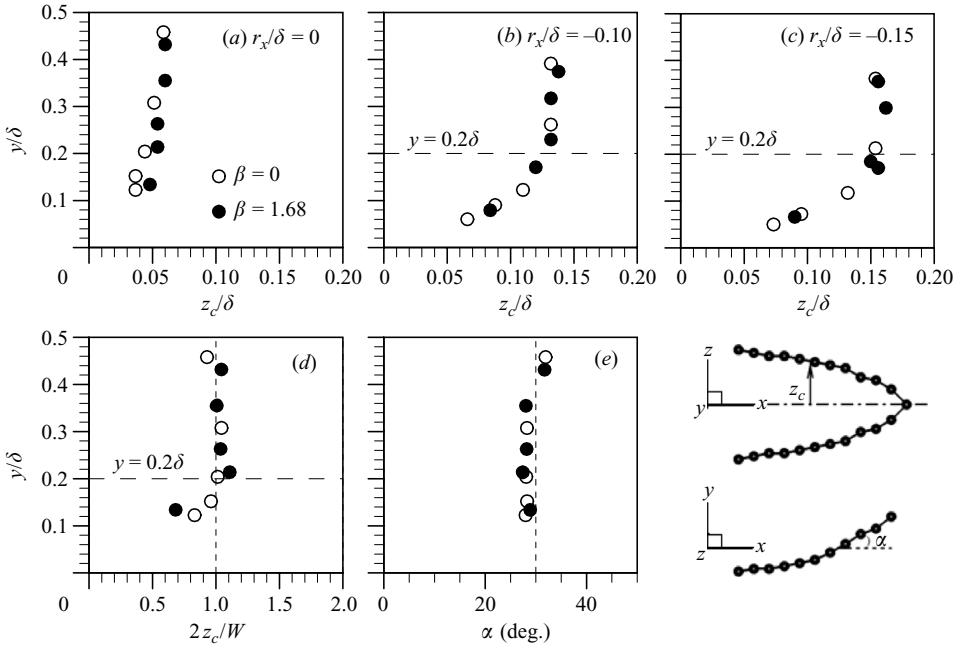

FIGURE 24. Loci of vortex centres at (*a*) $r_x/\delta = 0$, (*b*) $r_x/\delta = -0.1$ and (*c*) $r_x/\delta = -0.15$. (*d*) Ratio of spanwise spacing between vortex cores at $r_x/\delta = -0.1$ to the width of the LMR. (*e*) Inclination angle of the vortex leg in the vertical plane, α.

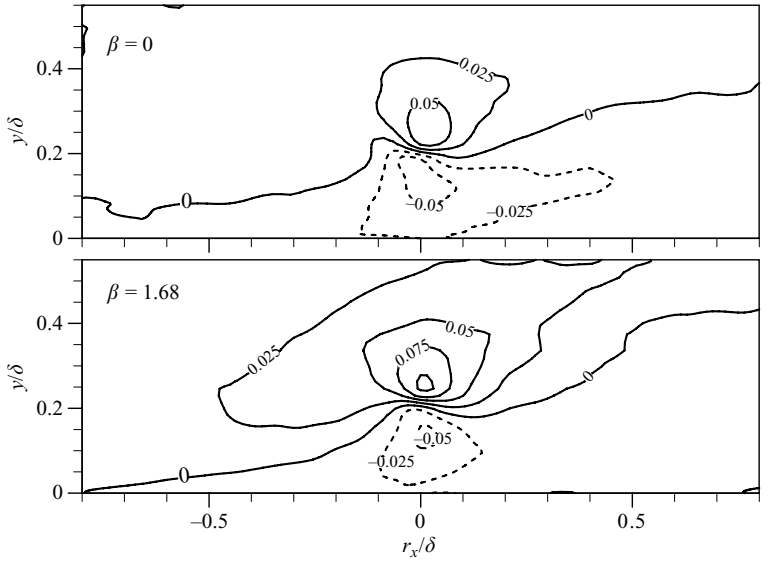

FIGURE 25. Two-point correlations between the streamwise velocity and the swirling strength for $y/\delta = 0.2$. Contour levels are from −0.05 to 0.1 with increments of 0.025.

4.4.1. *Two-point correlations between swirling strength and velocity*

Figure 25 shows the contours of the two-point correlations between swirling strength and streamwise velocity $R_{\lambda u}$ at $y/\delta = 0.2$. Figure 26 shows the wall-normal

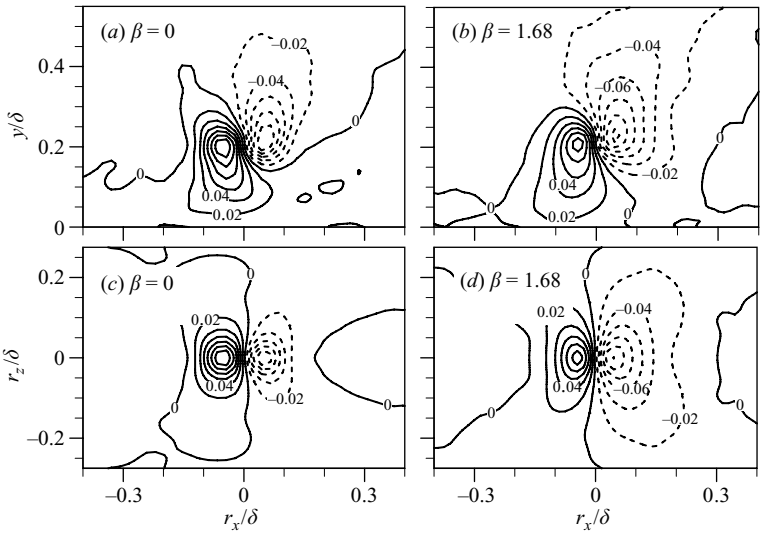

FIGURE 26. Two-point correlations between the wall-normal velocity and the swirling strength centred at $y/\delta = 0.2$: x–y plane at $r_z = 0$, (*a*) $\beta = 0$ and (*b*) $\beta = 1.68$; x–z plane at $y/\delta = 0.2$, (*c*) $\beta = 0$ and (*d*) $\beta = 1.68$. Contour levels are from -0.12 to 0.12 with increments of 0.02.

correlation functions $R_{\lambda v}$ for the same location. The present streamwise and wall-normal correlation functions for the ZPG flow are qualitatively consistent with those of Christensen & Adrian (2001), which were obtained from channel data. The contours of correlation show the average velocity field associated with a vortex core located at the reference point. Since the swirling strength always has a positive or zero value, $R_{\lambda u}$ and $R_{\lambda v}$ have the same sign as the streamwise and wall-normal velocities respectively. Thus, the statistically dominant direction of rotation around the vortex core can be determined from the two-point correlations between swirling strength and velocity. In the x–y plane, $R_{\lambda u}$ is positive above the vortex core and negative below the vortex core; $R_{\lambda v}$ is positive left of $r_x^+ = 0$ and negative right of $r_x^+ = 0$ for both the APG and ZPG flows; i.e. the rotation in the spanwise vortices is clockwise. This result implies that spanwise vortices with clockwise rotation are detected in this region more often than those with counterclockwise rotation, which is consistent with the instantaneous visualizations.

When a strong APG is applied, the spatial extents of the negative $R_{\lambda v}$ regions behind the vortex cores increase. Note that the negative $R_{\lambda v}$ region expands towards the near-wall region for a strong APG flow, as can be seen in figure 26(*b*). This result indicates that the outer turbulence is transported further towards the wall for a strong APG flow and that this strong downward diffusion is associated with the spanwise vortex in the log layer; it also complements the experimental study of Skåre & Krogstad (1994), which shows that the direction of the turbulent diffusion is reversed, resulting in considerable turbulent transport towards the wall in the TBL near separation. Figures 26(*c*) and 26(*d*) show the contours of $R_{\lambda v}$ for ZPG and APG flows in the x–z plane at $y/\delta = 0.2$ respectively. The spanwise extent of negative $R_{\lambda v}$ contours for the APG flow is greater than that for the ZPG flow. This difference is linked to the increase in the spanwise extent of conditional eddies that results from the APG, as shown in figure 22(*b*). However, the change in the spanwise dimension of the positive $R_{\lambda v}$ region is less than that of the negative $R_{\lambda v}$ region because the

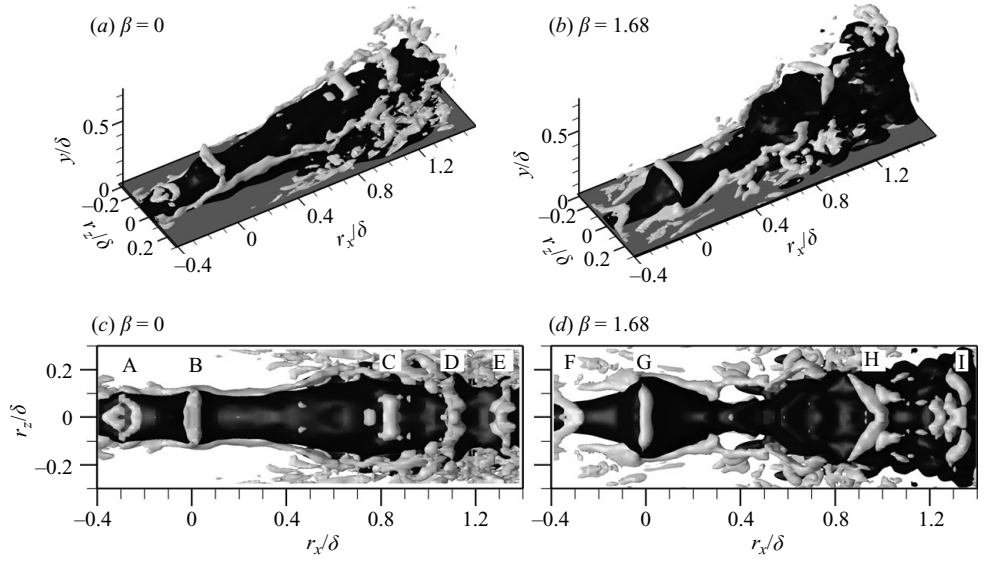

FIGURE 27. Vortex organization of the linearly estimated velocity field for a spanwise swirl at $y/\delta = 0.2$. Perspective view: (*a*) $\beta = 0$; (*b*) $\beta = 1.68$. Top view: (*c*) $\beta = 0$; (*d*) $\beta = 1.68$. The vortices are identified from the grey isosurface plots of λ_{ci}.

positive region (the Q2 event) is confined by the two legs of the hairpin vortex, and the distances in the APG and ZPG flows are similar, as shown in figure 23. The streamwise extent of the positive $R_{\lambda u}$ region is greater for the APG flow than for the ZPG flow. However, the streamwise extent of the negative $R_{\lambda u}$ region is reduced by the downward diffusion mentioned above. For streamwise correlation functions, the inclination angle of the 0-contours is an estimate of the average inclination angle of the outer vortex organization. The inclination angle of the APG flow is larger than that of the ZPG flow.

4.4.2. *Vortex organizations educed by LSE*

The stochastic estimation of the conditionally averaged velocity fields around the single spanwise vortex at $y/\delta = 0.2$ was performed using the correlation functions described in the previous section. The flow structures educed from the linear estimates are illustrated in figure 27. The velocity vectors in the estimated flow fields were set to unit magnitude in order to show the weak motions away from the event location more clearly (Christensen & Adrian 2001). The vortices were visualized using isosurfaces of λ_{ci} equal to 7 % and 10 % of its maximum for the ZPG and APG flows respectively. The dark area represents low-speed fluid. The resulting flow structures in the three-dimensional perspective are packets of hairpin-like vortices for both the ZPG ($\beta = 0$) and APG ($\beta = 1.68$) flows, as shown in figures 27(*a*) and 27(*b*) respectively. It is clear that the spanwise-oriented vortex structure is located at the event location, which corresponds to the head of the hairpin-type vortex. This hairpin-like vortex consists of two quasi-streamwise legs and a steeply inclined hairpin part. This result suggests that the dominant spanwise swirling motions in the log layer are associated with the hairpin head. The symmetry of the eddies is a consequence of the statistical symmetry of the given event with respect to the reflection about the vertical plane at $r_z^+ = 0$. Of course, most individual structures have asymmetric shapes, as shown in figure 14.

Spanwise vortex structures are visible not only at the event location but also both upstream and downstream of this location. This result implies that the vortices are arranged in the streamwise direction with considerable coherence. There is a qualitative similarity between the averaged vortex organization (figure 27) and the instantaneous realizations (figure 14). Five and four distinct hairpin-like vortices form packets in the ZPG and APG flows respectively and are aligned in the streamwise direction. It is interesting to note that the hairpin legs survive the averaging process even though the streamwise alignment of the hairpin in each packet is not perfect and the spanwise size of the packets varies from packet to packet. A little noise is present in the isosurface of λ_{ci} away from the event point, since the packets in the instantaneous fields are not perfectly aligned in the streamwise direction and the ensembles are not fully converged. However, the ensembles can be used to identify the spanwise vortex structures. There is an elongated LMR beneath the streamwise hairpin packet that is bounded by hairpin vortices. These patterns are consistent with the hairpin vortex packet model of Adrian *et al.* (2000). For $\beta = 0$, compact spanwise vortex structures can be seen, as shown in figure 27(*c*) (marked A and C). Zhou *et al.* (1999) observed similar spanwise vortices located between quasi-streamwise vortices and showed that compact spanwise vortices assist the uplift of quasi-streamwise vortices and that the spanwise vortex is then connected with the lifted streamwise vortices. For $\beta = 1.68$, the spanwise extents of the hairpin vortices located at $y/\delta > 0.2$ are relatively insensitive to the distance from the wall. The spanwise extent is about 0.4δ, as shown in figure 27(*d*).

The velocity vector fields on the x–y plane at $r_z = 0$ for the ZPG and APG flows are shown in figures 28(*a*) and 28(*b*) respectively. The locations of the vortex cores are indicated by the swirling strength contours. It is clear that upward motion of low-speed fluid (Q2) is observed just upstream of and below the vortex core at the event location for both flows. For $\beta = 1.68$, a downward motion of high-speed fluid (Q4) that is stronger than that for $\beta = 0$ appears just behind the vortex core. Spanwise swirling motions are visible not only at the specified event location but also both upstream and downstream of this location. For $\beta = 0$, the vortical motions are inclined away from the wall at an angle of 13°. This result is consistent with the observations of Zhou *et al.* (1999) and Christensen & Adrian (2001). For $\beta = 1.68$, the inclination angle is approximately 18.5°, which is larger than that for $\beta = 0$. These inclination angles are consistent with the instantaneous realizations in figure 17.

For $\beta = 0$, the streamwise separation of the vortex cores varies with the distance from the wall. The streamwise distance between the vortex cores A and B is approximately 150 viscous wall units (0.23δ). This separation is similar to the experimentally observed streamwise separation between hairpin heads within a packet of 100–200 viscous wall units (Adrian *et al.* 2000). Away from the wall, the vortex cores B and C are separated by approximately 550 viscous wall units (0.83δ). Adrian *et al.* (2000) reported that the vortex spacing is governed by inner scales but increases as the hairpins grow. In contrast, Christensen & Adrian (2001) showed that the average vortex spacing can be scaled with the outer length scale δ regardless of the Reynolds number, with a spacing of approximately 0.3–0.4δ. The spacing is approximately half of the vortex spacing between B and C. The vortex spacing is in good agreement with the results of Christensen & Adrian (2001), except for the region between B and C; they noted that the swirling motion 0.4δ downstream from the event location is not clear. The increased spacing between vortex cores found in the present data might be the result of a vortex that is missing due to the variation of the vortex spacing from packet to packet during the averaging process, as suggested in Christensen & Adrian

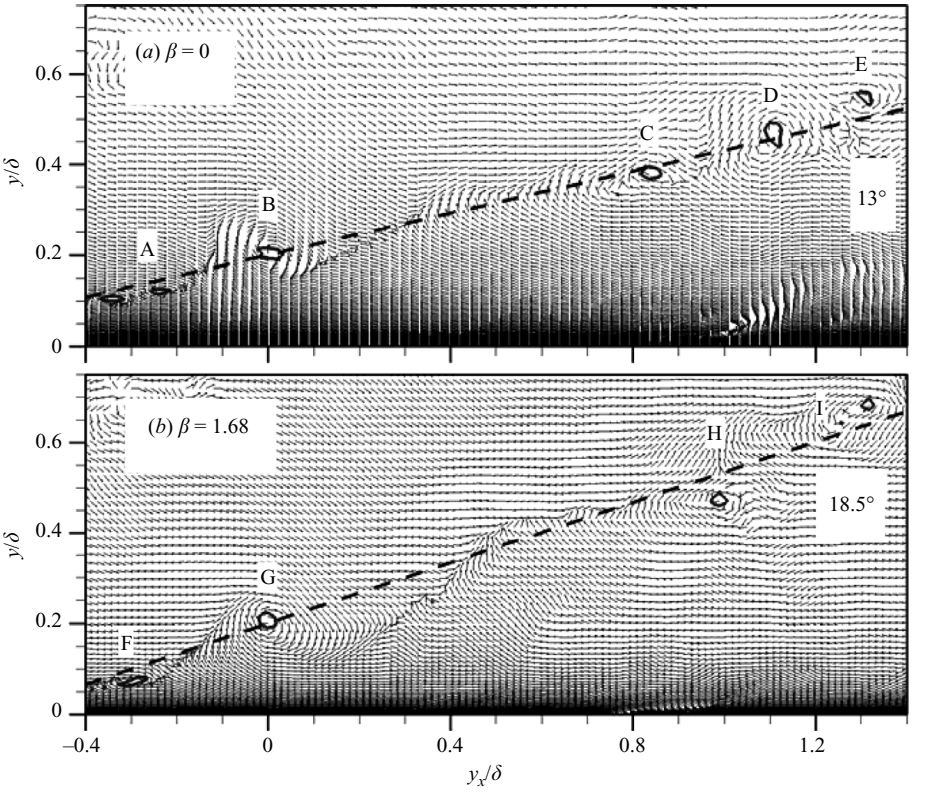

FIGURE 28. Linear estimate of the conditional velocity field based on a spanwise swirl at $y/\delta = 0.2$. The locations of the vortex cores are indicated by the swirling strength contours.

(2001). However, the swirling patterns of the downstream vortices C, D and E are clear. The streamwise spacings between C and D and between D and E are approximately 0.28δ and 0.2δ respectively, which are similar to the distance between A and B. These streamwise separations are also similar to the streamwise dimensions of the individual outer conditional eddies. These results suggest that vortices A and C are secondary vortices generated upstream of the primary vortices B and D respectively, as reported in Zhou, Adrian & Balachandar (1996), and that the hairpin spacing is governed by both inner and outer variables. The streamwise spacing between the primary and secondary vortices is governed by small scales associated with the streamwise dimensions of individual hairpins, whereas the distance between the primary vortices B and D is governed by large scales associated with the streamwise dimensions of packets.

The qualitative similarity of the vortex spacing in the APG and ZPG flows is clear. However, the vortex spacing increases when the length scale is normalized by δ, as shown in figure 28(*b*). The streamwise vortex spacing in a packet is related to the frequency of strong Q2 events. Multiple Q2 events can occur within a single burst event (Bogard & Tiederman 1986). A single burst event is associated with the passage of a hairpin head in a packet (Adrian *et al.* 2000). If the spacing of vortex heads increases (respectively decreases), the frequency of the Q2 events associated with hairpin-like vortices decreases (respectively increases). Krogstad & Skåre (1995) reported that the frequency of Q2 events scaled with outer scaling is reduced and

that Q4 events last much longer in the APG flow than in the ZPG flow, in particular for strong events in APG TBLs. This reduction in the frequency of Q2 events can be explained in terms of increases in the streamwise spacing of hairpins in the conditionally averaged packets of the APG flow. The longer durations of Q4 events in the APG flow is related to the increased streamwise extent of the negative $R_{\lambda u}$ region just behind the vortex head.

5. Summary and conclusions

The effects of APGs on the structures of TBLs have been investigated. A comparison of the structures of ZPG TBLs and APG TBLs has been presented. When a strong APG is applied, near-wall streaks are weakened; the spanwise spacing between the streaks becomes irregular and increases significantly up to 400 viscous wall units, approximately four times larger than that of the ZPG flow, whereas the width of the streaks is relatively insensitive to the strength of the pressure gradient. A streamwise-elongated LMR is the predominant structure in the log layer. LSE of the conditional average based on a low-speed event was used to show that LMRs containing strong velocity fluctuations are present in the middle of the APG boundary layer as well as in the log layer, in contrast to the ZPG flow. Enhancements of the outer kinetic energy and the Reynolds shear stress are associated with the presence of large-scale outer streaky structures in APG TBLs. The average shape of the LMRs is less elongated and grows linearly with distance from the wall in the log layer. Beyond the log layer, the size of this region is approximately constant until $y/\delta = 0.6$, whereas the size of this region in the ZPG flow increases slightly.

The modifications of the vortical structures that result from the APG were examined by using linear estimates of the conditional eddies around the Q2 event that makes the largest contribution to the mean Reynolds shear stress. For a conditional event at $y^+ = 5.5$, the conditional eddies were found to be quasi-streamwise vortices. The mean diameter and the streamwise length normalized by inner scales are probably insensitive to the strength of the pressure gradient. The p.d.f.s of the streamwise vorticity show that the near-wall streamwise vorticity fluctuations of both flows normalized by their root-mean-square values are nearly identically distributed. However, the swirling motions of individual vortices in the streamwise direction are stronger for the APG flow than for the ZPG flow. For a conditional event at $y^+ > 50$, the conditional eddies take the form of hairpin-like vortices. Hairpin-like vortices are the dominant structures associated with the production of outer Reynolds shear stress. The swirling motion of each individual hairpin in the outer region is stronger for the APG flow than for the ZPG flow. For the conditional event in the log layer, the inclination angle of the vortex leg increases when an APG is applied. Beyond the log layer, the backbone of the steeply inclined part of each conditional eddy has a Λ shape with dimensions governed by the outer variables. The Λ shapes found in the two cases are similar when the length scales are normalized by the boundary layer thickness. Beyond $y = 0.2\delta$, the inclination angle of this part in the vertical plane is roughly constant at 30°, and the spanwise separation at the upstream end of the eddies is constant, approximately 0.4δ, which is in good agreement with the width of the LMR. The width of this large-scale outer structure is closely associated with the spanwise size of the conditional eddies in the outer region. Two-point correlations between the swirling strength and the velocity show that the outer turbulence is transported

further towards the wall just behind the spanwise vortex core in the presence of an APG.

Finally, the present results provide the first three-dimensional evidence for packets of hairpin-type vortices in TBLs and are based on linear stochastic estimation of the conditionally averaged flow field associated with a single transverse vortex core. The outer region of the TBL is populated with streamwise packets of vortices. Although it may be not possible to detect all hairpins on a packet through the current analysis, the packet of vortices is sufficiently significant in the outer region of the APG to leave a footprint on the results of the conditional average. The vortices are relatively well aligned in the streamwise direction and convect coherently behind each other. The APG augments the angle of inclination of the packets and the spacing of the vortex heads. The increase in the streamwise vortex spacing explains the reduction in the frequency of Q2 events. We believe that the typical characteristics of a hairpin packet are present in an average sense, since multiple hairpin heads and legs in a packet survive the conditional averaging, despite variations in the hairpin arrangement in the instantaneous vortex packets. Studies of much higher Reynolds numbers are needed to determine the overall behaviour of hairpin packets, since the packets at low Reynolds numbers contain just 3–5 vortices.

This work was supported by the Creative Research Initiatives of the Korea Science & Engineering Foundation and was partially supported by the Korea Institute of Science and Technology Information under the Grand Challenge Supercomputing Program.

REFERENCES

Acarlar, M. S. & Smith, C. R. 1987 A study of hairpin vortices in a laminar boundary layer. Part 2. Hairpin vortices generated by fluid injection. *J. Fluid Mech.* **175**, 43–83.

Adrian, R. J. 2007 Hairpin vortex organization in wall turbulence. *Phys. Fluids* **19**, 041301.

Adrian, R. J., Jones, B. G., Chung, M. K., Hassan, Y., Nithianandan, C. K. & Tung, A. T. C. 1989 Approximation of turbulent conditional averages by stochastic estimation. *Phys. Fluids* A **1**, 992–998.

Adrian, R. J., Meinhart, C. D. & Tomkins, C. D. 2000 Vortex organization in the outer region of the turbulent boundary layer. *J. Fluid Mech.* **422**, 1–54.

Adrian, R. J. & Moin, P. 1988 Stochastic estimation of organized turbulent structure: homogeneous shear flow. *J. Fluid Mech.* **190**, 531–539.

Aubry, N., Holmes, P., Lumley, J. L. & Stone, E. 1988 The dynamics of coherent structures in the wall region of a turbulent boundary layer. *J. Fluid Mech.* **192**, 115–173.

Bandyopadhyay, P. 1980 Large structure with a characteristic upstream interface in turbulent boundary layers. *Phys. Fluids* **23**, 2326–2327.

Bogard, D. G. & Tiederman, W. G. 1986 Burst detection with single-point velocity measurements. *J. Fluid Mech.* **76**, 89–112.

Christensen, K. T. & Adrian, R. J. 2001 Statistical evidence of hairpin vortex packets in wall turbulence. *J. Fluid Mech.* **431**, 433–443.

De Graaff, D. B. & Eaton, J. K. 2000 Reynolds-number scaling of the flat-plate turbulent boundary layer. *J. Fluid Mech.* **422**, 319–346.

Finnicum, D. S. & Hanratty, T. J. 1988 Effect of favourable pressure gradients on turbulent boundary layers. *AIChE J.* **34** (4), 529–540.

Ganapathisubramani, B., Longmire, E. K. & Marusic, I. 2003 Characteristics of vortex packets in turbulent boundary layers. *J. Fluid Mech.* **478**, 35–46.

Head, M. R. & Bandyopadhyay, P. 1981 New aspects of turbulent boundary-layer structure. *J. Fluid Mech.* **107**, 297–338.

Houra, T., Tsuji, T. & Nagano, Y. 2000 Effects of adverse pressure gradient on quasi-coherent structures in turbulent boundary layer. *Intl J. Heat Fluid Flow* **21** (3), 304–311.

Hutchins, N., Hambleton, W. T. & Marusic, I. 2005 Inclined cross-stream stereo particle image velocimetry measurements in turbulent boundary layers. *J. Fluid Mech.* **541**, 21–54.

Jeong, J., Hussain, F., Schoppa, W. & Kim, J. 1997 Coherent structures near the wall in a turbulent channel flow. *J. Fluid Mech.* **332**, 185–214.

Kim, K., Baek, S. J. & Sung, H. J. 2002 Animplicit velocity decoupling procedure for the incompressible Navier–Stokes equations. *Intl J. Numer. Meth. Fluids* **38**, 125–138.

Kim, J., Moin, P. & Moser, R. 1987 Turbulence statistics in fully developed channel flow at low Reynolds number. *J. Fluid Mech.* **177**, 133–166.

Kim, K., Sung, H. J. & Adrian, R. J. 2008 Effects of background noise on generating coherent packets of hairpin vortices. *Phys. Fluids* **20**, 105107.

Kline, S. J., Reynolds, W. C., Schraub, F. A. & Runstadler, P. W. 1967 The structure of turbulent boundary layers. *J. Fluid Mech.* **30**, 741–773.

Kline, S. J. & Robinson, S. K. 1989 Quasi-coherent structures in the turbulent boundary layer. Part 1. Status report on a community-wide summary of the data. In *Near Wall Turbulence* (ed. S. J. Kline & N. H. Afgan), pp. 218–247. Hemisphere.

Krogstad, P. & Skåre, P. E. 1995 Influence of a strong adverse pressure gradient on the turbulent structure in a boundary layer. *Phys. Fluids* **7**, 2014–2024.

Lee, J.-H. & Sung, H. J. 2008 Effects of an adverse pressure gradient on a turbulent boundary layer. *Intl J. Heat Fluid Flow* **29** (3), 568–578.

Lund, T. S., Wu, X. & Squires, K. D. 1998 Generation of turbulent inflow data for spatially-developing boundary layer simulations. *J. Comput. Phys.* **140** (2), 233–258.

Marusic, I. & Perry, A. E. I. 1995 A wall-wake model for the turbulence structure of boundary layers. Part 2. Further experimental support. *J. Fluid Mech.* **298**, 389–407.

Marusic, I. 2001 On the role of large-scale structures in wall turbulence. *Phys. Fluids* **13**, 735.

Mellor, G. L. & Gibson, D. M. 1966 Equilibrium turbulent boundary layers. *J. Fluid Mech.* **24**, 225–253.

Moin, P., Adrian, R. J. & Kim, J. 1987 Stochastic estimation of organized structures in turbulent channel flow. In *Proceedings of the Sixth Turbulent Shear Flow Symposium*, Toulouse, France, pp. 16.9.1–16.9.8.

Na, Y. & Moin, P. 1998 The structure of wall-pressure fluctuations in turbulent boundary layers with adverse pressure gradient and separation. *J. Fluid Mech.* **377**, 347–373.

Nagano, Y., Tagawa, M. & Tsuji, T. 1993 Effects of adverse pressure gradients on mean flows and turbulence statistics in a boundary layer. In *Turbulent Shear Flows 8* (ed. F. Durst, R. Friedrich, B. E. Launder, F. W. Schmidt, U. Schumann & J. H. Whitelaw), pp. 7–21. Springer.

Perry, A. E., Henbest, S. & Chong, M. S. 1986 A theoretical and experimental study of wall turbulence. *J. Fluid Mech.* **165**, 163–199.

Perry, A. E. & Marusic, I. 1995 A wall-wake model for the turbulence structure of boundary layers. Part 1. Extension of the attached eddy hypothesis. *J. Fluid Mech.* **298**, 361–388.

Robinson, S. K. 1991 Coherent motions in the turbulent boundary layer. *Annu. Rev. Fluid Mech.* **23**, 601–639.

Skåre, P. E. & Krogstad, P. A. 1994 A turbulent equilibrium boundary layer near separation. *J. Fluid Mech.* **272**, 319–348.

Skote, M. & Henningson, D. 2002 Direct numerical simulation of a separated turbulent boundary layer. *J. Fluid Mech.* **471**, 107–136.

Skote, M., Henningson, D. S. & Henkes, R. 1998 Direct numerical simulation of self-similar turbulent boundary layers in adverse pressure gradients. *Flow Turbul. Combust.* **60**, 47–85.

Smith, C. R. & Metzler, S. P. 1983 The characteristics of low-speed streaks in the near-wall region of a turbulent boundary layer. *J. Fluid Mech.* **129**, 27–54.

Smith, C. R., Walker, J. D. A., Haidari, A. H. & Sobrun, U. 1991 On the dynamics of near-wall turbulence. *Phil. Trans. R. Soc. Lond.* A **336** (1641), 131–175.

Theodorsen, T. 1952 Mechanism of turbulence. In *Proceedings of the Second Midwestern Conference on Fluid Mechanics*, Ohio State University, Columbus, OH, pp. 1–19.

Tomkins, C. D. & Adrian, R. J. 2003 Spanwise structure and scale growth in turbulent boundary layers. *J. Fluid Mech.* **490**, 37–74.

Townsend, A. A. 1961 Equilibrium layers and wall turbulence. *J. Fluid Mech.* **11**, 97–120.

Zhou, J., Adrian, R. J. & Balachandar, S. 1996 Autogeneration of near-wall vortical structures in channel flow. *Phys. Fluids* **8**, 288.

Zhou, J., Adrian, R. J., Balachandar, S. & Kendall, T. M. 1999 Mechanisms for generating coherent packets of hairpin vortices in channel flow. *J. Fluid Mech.* **387**, 353–396.